


RESEARCH ARTICLE

Open Access



# An extensional strain sensing mechanosome drives adhesion-independent platelet activation at suprphysiological hemodynamic gradients

Nurul A. Zainal Abidin<sup>1</sup>, Eric K. W. Poon<sup>2</sup>, Crispin Szydzik<sup>1,3</sup>, Mariia Timofeeva<sup>4†</sup>, Farzan Akbaridoust<sup>4†</sup>, Rose J. Brazilek<sup>1</sup>, Francisco J. Tovar Lopez<sup>3</sup>, Xiao Ma<sup>5</sup>, Chitrarth Lav<sup>4,6</sup>, Ivan Marusic<sup>4</sup>, Philip E. Thompson<sup>5</sup>, Arnan Mitchell<sup>3</sup>, Andrew S. H. Ooi<sup>4</sup>, Justin R. Hamilton<sup>1</sup> and Warwick S. Nesbitt<sup>1\*</sup> 

## Abstract

**Background:** Suprphysiological hemodynamics are a recognized driver of platelet activation and thrombosis at high-grade stenosis and in blood contacting circulatory support devices. However, whether platelets mechano-sense hemodynamic parameters directly in free flow (in the absence of adhesion receptor engagement), the specific hemodynamic parameters at play, the precise timing of activation, and the signaling mechanism(s) involved remain poorly elucidated.

**Results:** Using a generalized Newtonian computational model in combination with microfluidic models of flow acceleration and quasi-homogenous extensional strain, we demonstrate that platelets directly mechano-sense acute changes in free-flow extensional strain independent of shear strain, platelet amplification loops, von Willebrand factor, and canonical adhesion receptor engagement. We define an extensional strain sensing “mechanosome” in platelets involving cooperative  $\text{Ca}^{2+}$  signaling driven by the mechanosensitive channel Piezo1 (as the primary strain sensor) and the fast ATP gated channel P2X1 (as the secondary signal amplifier). We demonstrate that type II PI3 kinase C2 $\alpha$  activity (acting as a “clutch”) couples extensional strain to the mechanosome.

**Conclusions:** Our findings suggest that platelets are adapted to rapidly respond to suprphysiological extensional strain dynamics, rather than the peak magnitude of imposed wall shear stress. In the context of overall platelet activation and thrombosis, we posit that “extensional strain sensing” acts as a priming mechanism in response to threshold levels of extensional strain allowing platelets to form downstream adhesive interactions more rapidly under the limiting effects of suprphysiological hemodynamics.

**Keywords:** Platelet, Hemodynamics, Mechanotransduction, Extensional strain

## Background

Blood platelets are anucleate cells derived from megakaryocytes that are central to physiological hemostasis and are a key player in pathological thrombosis. Mechanical hemodynamic parameters are major drivers of both physiological and pathological platelet function. At sites of arterial stenosis, associated with atherosclerotic disease, or within blood contacting mechanical circulatory support (MCS) and extracorporeal membrane oxygenation

\*Correspondence: warwick.nesbitt@monash.edu

†Mariia Timofeeva and Farzan Akbaridoust contributed equally to this work.

<sup>1</sup>The Australian Centre for Blood Diseases, Monash University, Melbourne, VIC 3004, Australia

Full list of author information is available at the end of the article



(ECMO) circuits, platelets can experience a wide array of mechanical forces that impact their function, including elevated wall strain rates ( $\dot{\gamma}$ ) and local fluid stresses ( $\tau$ ) [1, 2], mass transport phenomena due to erythrocyte margination effects and flow recirculation [3], tensile and compressive forces upon impact and adhesion at sites of subendothelial matrix exposure and artificial device surfaces [4, 5], velocity gradients, and extensional (elongational) strain due to flow acceleration [6–8]. Platelets transduce these external mechanical stimuli into specific intracellular biochemical signals (mechanotransduction) that include,  $[Ca^{2+}]_c$  flux [9] phosphoinositide synthesis [10, 11], cytoskeletal remodeling [12], and adhesion receptor engagement, activation, and signaling [13]. These processes drive platelet functional outputs, such as surface translocation, membrane tethering [6, 14], shape (morphology) change, shear-induced platelet aggregation (SIPA), and ultimately thrombus formation.

SIPA occurs when platelets convected in bulk flow aggregate upon contact with surface immobilized von Willebrand factor (VWF) and/or activated co-adhered platelets.  $\dot{\gamma}$  is a critical hemodynamic parameter that regulates platelet capture from free flow, aggregation rate, and size [15]. We and others have demonstrated that platelet aggregation in the presence of VWF occurs within relatively low  $\dot{\gamma}$  zones just downstream from sites of high  $\dot{\gamma}$  [6]. Significantly, these studies demonstrated that the early stages of SIPA involve resting discoid platelets through the formation of passive membrane tether structures [6] in association with platelet GPIb/V/IX binding to shear ( $\tau \geq 3.5$  to 5.0 Pa) decrypted VWF [6, 16, 17]. Initial engagement of these membrane tethers is followed by transient  $[Ca^{2+}]_c$  flux and correlated active tether restructuring and aggregate consolidation [6]. Classical amplification loop signaling mediated by platelet and red blood cell (RBC) secretion of ATP, ADP,  $TXA_2$ , and thrombin generation subsequently stabilize forming aggregates in the face of destabilizing high  $\tau$  [18]. Significantly, when platelet amplification loops are inhibited or where flow-dependent advective clearance rates are high, elevated  $\tau$  can destabilize and limit aggregate consolidation leading to embolization. While these findings indicate that stable platelet aggregation preferentially occurs in flow sheltered zones downstream from regions of flow acceleration, little to no evidence has been forthcoming as to whether platelets “mechano-sense” the initial free-flow acceleration phase, and how this may influence the rate of downstream membrane tethering, aggregation, and thrombus formation.

There is a clear knowledge gap with respect to how supraphysiological velocity gradients, as seen at severe stenosis or due to MCS/ECMO pump operation and fluidic circuits, impact platelet activation dynamics and

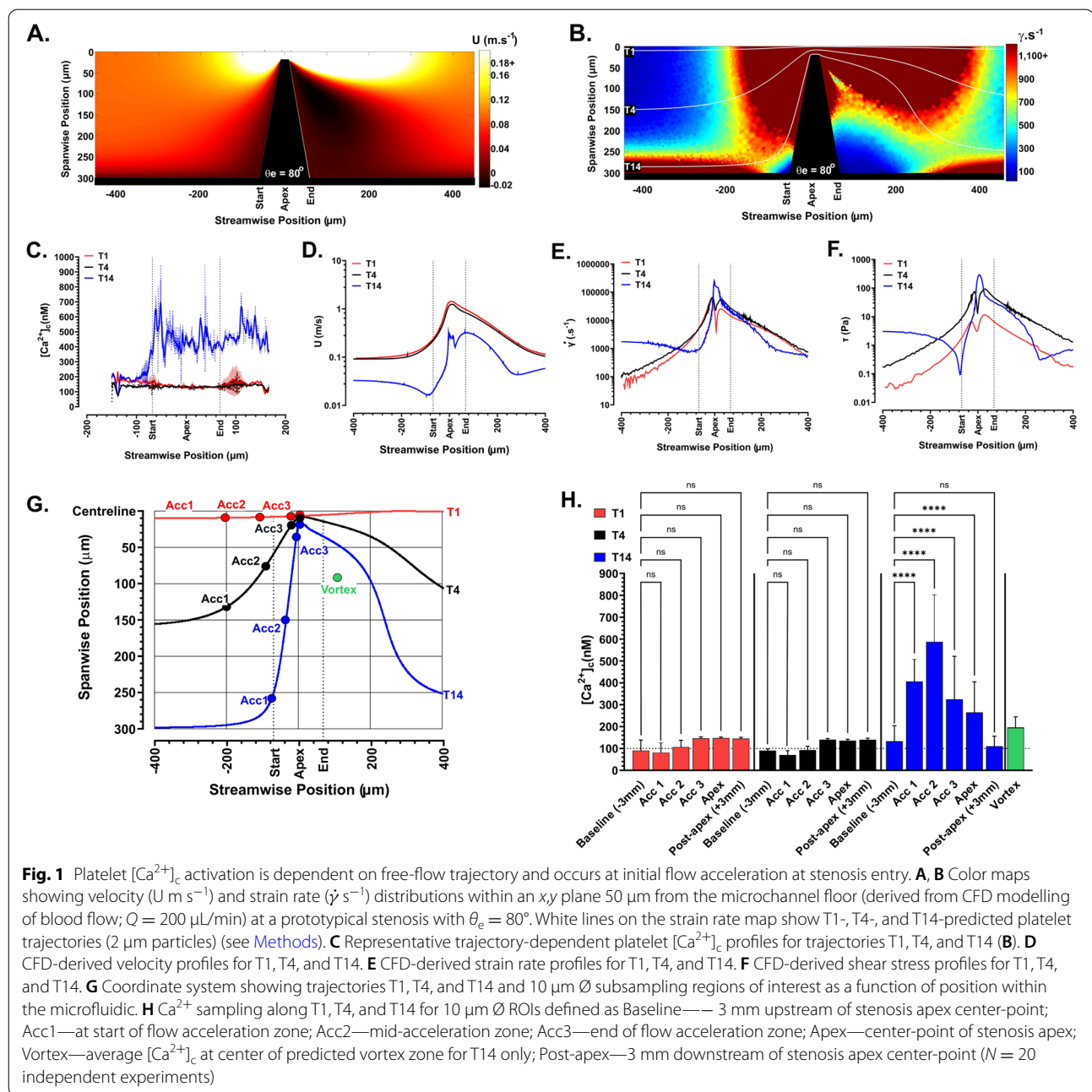
functional behavior. To that end, and to isolate free-flow velocity effects from adhesion-mediated platelet activation events, we developed and employed a generalized Newtonian computational fluid dynamics (CFD)-directed microfluidics and time-averaged  $[Ca^{2+}]_c$  imaging approach to investigate the effects of supraphysiological free-flow acceleration on platelet function. We identify a critical role for extensional strain at flow acceleration in directly modulating platelet mechanotransduction in the absence of adhesion receptor engagement. Through a series of pharmacologic inhibition and activation studies, we identify a novel “extensional strain sensing mechanosome” that primes platelets for immediate downstream platelet aggregation at supraphysiological velocity gradients.

## Results

### Platelets exhibit $[Ca^{2+}]_c$ transients in response to supraphysiological flow acceleration independent of canonical adhesion and agonist-dependent signaling

To investigate the impact of supraphysiological hemodynamics on platelet activation, we utilized a set of stenosis microfluidic geometries designed to subject blood/platelets to supraphysiological velocity gradients dependent on flow rate ( $Q$ ) and streamwise trajectory. This microfluidic assay allowed for exposure of whole or reconstituted human blood to defined flow velocity gradients in the absence of platelet-surface adhesion or plasma protein interactions (Additional file 1: Fig. S1). By specifically controlling stenosis entry angle ( $\theta_e$ ), we were able to modulate blood flow acceleration while maintaining peak velocity at the stenosis apex and maintaining constant downstream velocities. Initial CFD modelling of blood flow (see “Methods”) for a prototypical stenosis geometry with  $\theta_e = 80^\circ$ , designed to subject blood/platelet samples to a maximal velocity gradient of 0.01 to 1 m s<sup>-1</sup> at  $Q = 200$   $\mu$ L/min (Fig. 1A), predicted a highly heterogeneous strain rate field with manifest zones of low  $\dot{\gamma} \leq 100$  s<sup>-1</sup> and adjacent zones of elevated  $\dot{\gamma} \geq 100,000$  s<sup>-1</sup>; proximal to the upstream face of stenosis entry (Fig. 1B & Additional file 1: Fig. S2A & B). CFD particle tracing ( $Q = 200$   $\mu$ L/min) predicted that platelets will experience distinct velocity and strain rate profiles determined by their spanwise position on release (Fig. 1B & Additional file 1: Fig. S2A). Platelet trajectories were qualitatively confirmed by time-averaged imaging of CytoTracker® Green-labelled human platelets reconstituted with RBC at a hematocrit of 40% perfused through the  $\theta_e = 80^\circ$  geometry at  $Q = 200$   $\mu$ L/min (Additional file 1: Fig. S2C).

Based on our CFD modelling data, we hypothesized that platelets would exhibit activation states dictated by their streamwise trajectory and correlated hemodynamic profile. To test this hypothesis, we conducted



time-averaged confocal platelet  $Ca^{2+}$  imaging (see “*Methods*”) of reconstituted blood samples at  $Q = 200\ \mu L/min$ . We interrogated this imaging data by mapping a subset of CFD predicted trajectories onto the imaging data (see “*Methods*”) and analyzed platelet  $[Ca^{2+}]_c$  profiles as a function of predicted trajectory. Figure 1C shows platelet  $[Ca^{2+}]_c$  flux profiles for sample trajectories designated T1, T4, and T14 (chosen as representative centerline, mid-span, and near wall trajectories (Fig. 1B)) and demonstrates that platelets tracking within  $10\ \mu m$  of

the sidewall (T14) exhibit a significant  $[Ca^{2+}]_c$  flux initiating at the start of flow acceleration, while platelets within trajectories approaching mid-span and centerline (T4 and T1) showed no change in  $[Ca^{2+}]_c$  above baseline. Correlated interrogation of trajectory-specific hemodynamic profiles demonstrated that trajectories within  $10\ \mu m$  of the sidewall (T14) display an initial velocity ( $U$ ), strain rate ( $\dot{\gamma}$ ), and shear stress ( $\tau$ ) “inflection point,” typified by a marked reduction in all three parameters followed by a rapid upstroke (Fig. 1D–F). This

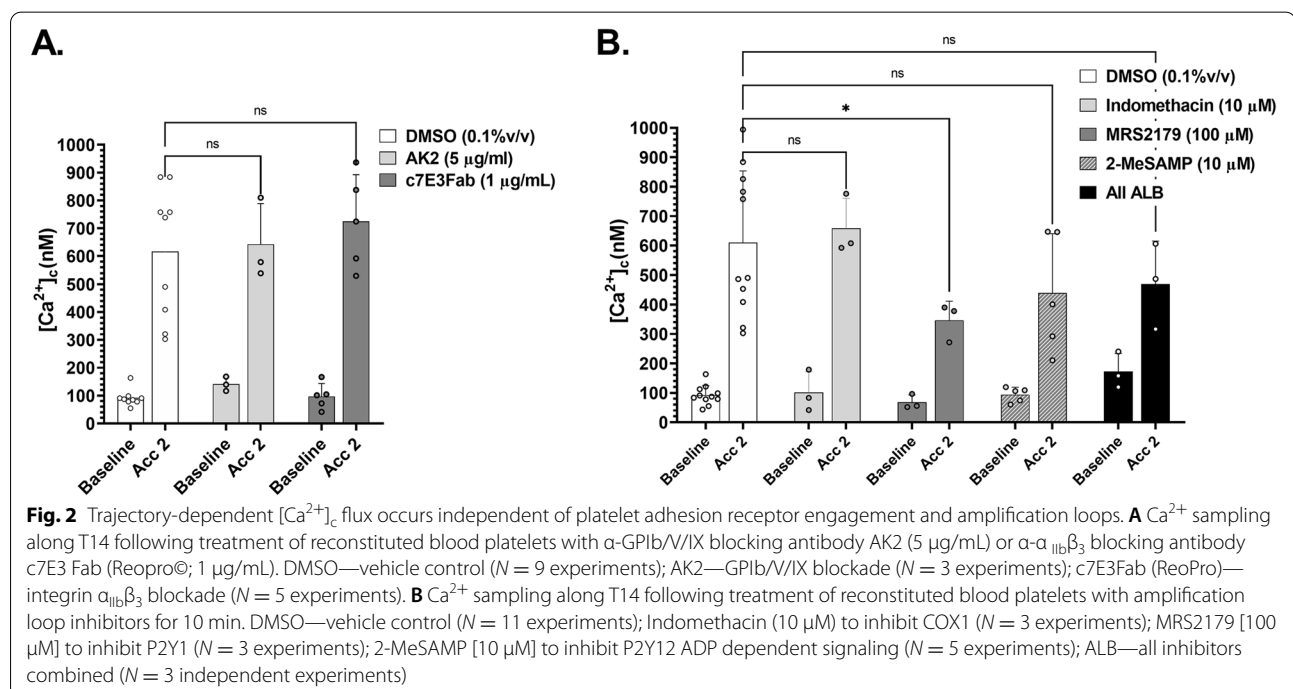
hemodynamic “inflection point” occurred at the start of the acceleration phase and was congruent with initiation of platelet  $[Ca^{2+}]_c$  flux (Fig. 1C–F). Mid-span and centerline trajectories (T4 and T1) did not show this hemodynamic behavior, with a relatively smooth transition in all hemodynamic parameters and no associated  $[Ca^{2+}]_c$  flux (Fig. 1C–F). Significantly, platelets tracking 10  $\mu\text{m}$  (T14) from the sidewall experience steady-state  $\dot{\gamma}$  and  $\tau$  prior to the acceleration phase  $\sim 20$  to  $\sim 80$ -fold higher than mid-span and centerline trajectories, suggesting that platelet  $[Ca^{2+}]_c$  flux is triggered by the perturbation of hemodynamics at flow acceleration rather than steady-state  $\dot{\gamma}$  and  $\tau$  magnitude per se.

To obtain a statistical overview of the acceleration phase  $Ca^{2+}$  signaling phenomenon, we subsampled designated regions of interest (ROI) (Fig. 1G) along T1, T4, and T14 for  $N = 20$  independent donor platelet samples (Fig. 1H). ROI sampling supported our single-profile studies (Fig. 1C) and indicated that T14 platelet  $[Ca^{2+}]_c$  flux was initiated at the start of the acceleration phase (Acc1), with a significant shift from baseline of  $\sim 100$  to  $\sim 408$  nM (Fig. 1H). Maximal  $[Ca^{2+}]_c$  was consistently reached at the relative midpoint of the acceleration phase (Acc2), with  $[Ca^{2+}]_c$  approaching  $\sim 587$  nM ( $\sim 6$ -fold increase over baseline) that was a function of input  $Q$  (Fig. 1H and Additional file 1: S2D). This midpoint  $[Ca^{2+}]_c$  maxima decreased approaching the stenosis apex, with peak  $[Ca^{2+}]_c$  at the end of the acceleration phase (Acc 3) approaching  $\sim 325$  nM (Fig. 1H). Significantly,

$[Ca^{2+}]_c$  at stenosis apex (where  $\dot{\gamma}$  and  $\tau$  reached maximum) was  $\sim 2.5$ -fold lower ( $\sim 235$  nM) than at mid-acceleration (Fig. 1H).  $[Ca^{2+}]_c$  at the center of the downstream flow vortex was  $\sim 199$  nM (Fig. 1H), with  $[Ca^{2+}]_c$  returning to baseline +3 mm post-apex (Fig. 1H). Supporting our single trajectory profiling data, T1 and T4 showed no significant change in platelet  $[Ca^{2+}]_c$  above baseline across their respective trajectories (Fig. 1H).

To eliminate a potential role for VWF binding interactions in mediating acceleration-dependent  $[Ca^{2+}]_c$  flux, we conducted a series of experiments in which GPIb/V/IX to VWF binding was blocked with the blocking antibody AK2 (5  $\mu\text{g}/\text{mL}$ ) [Invitrogen] and platelet integrin  $\alpha_{IIb}\beta_3$  binding was blocked with c7E3Fab (Reopro $^{\circ}$ ; 1  $\mu\text{g}/\text{mL}$ ). Neither AK2 nor c7E3Fab had any significant impact on acceleration-mediated platelet  $[Ca^{2+}]_c$  flux (Fig. 2A). Similarly, blockade of canonical platelet amplification loops had minimal to no effect on platelet  $[Ca^{2+}]_c$  flux under these conditions (Fig. 2B). Notably, platelet activation status as measured by integrin  $\alpha_{IIb}\beta_3$  activation (Pac1 binding) and P-selectin expression (AK-4), 6 mm post-stenosis apex, showed no significant elevation over baseline controls corroborating that acceleration-dependent platelet  $[Ca^{2+}]_c$  flux was highly localized to the hemodynamic gradient and short range in effect (Additional file 1: Fig. S2E).

Collectively, these data demonstrate that platelets exhibit an acute mechanotransduction response to



localized supraphysiological acceleration in free flow, independent of VWF and soluble agonist-mediated pathways. In addition, these data demonstrate that platelet activation is specifically dependent on platelet stream-wise trajectory and correlated hemodynamic profile at acceleration start.

#### Modification of acceleration profile directly modulates platelet $[Ca^{2+}]_c$ flux and aggregation dynamics

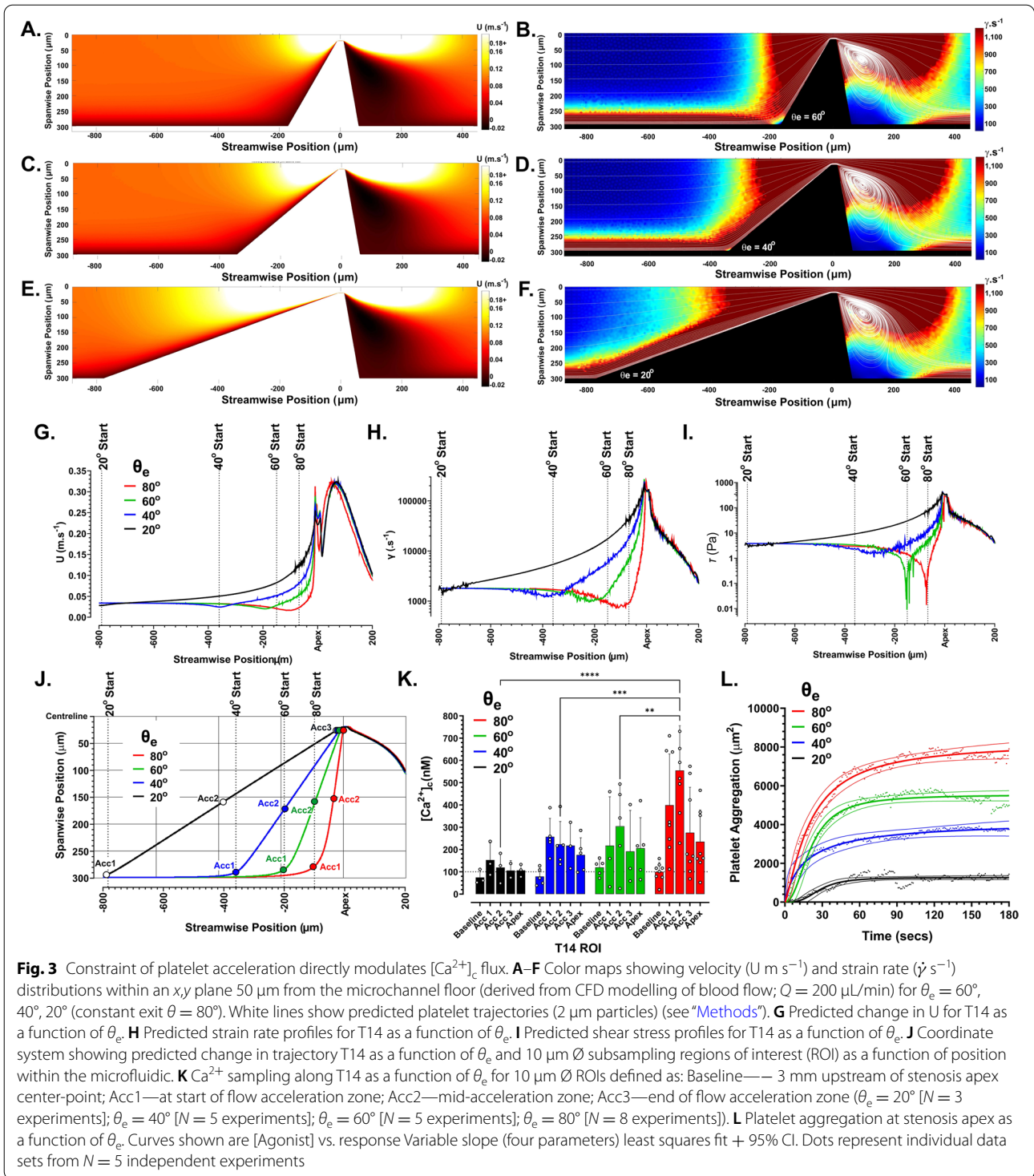
To further explore the way in which acceleration profile impacts platelet  $[Ca^{2+}]_c$  flux, we fabricated an additional series of symmetrical stenosis geometries with  $\theta_e$  varying from  $\theta_e = 20^\circ$ ,  $40^\circ$ , and  $60^\circ$  in order to progressively limit near wall (T14) acceleration in isolation from apex and downstream hemodynamics (Fig. 3A–F). CFD modelling of these geometries confirmed that  $\theta_e$ -dependent changes in the  $\dot{\gamma}$  field were isolated from downstream effects, such that  $\dot{\gamma}$  was equivalent at and downstream of the stenosis apex (Fig. 3A–F). CFD particle tracing also verified no significant change in apex-to-downstream platelet trajectories or vortex formation as a function of  $\theta_e$  (Fig. 3B, D & F). Changes in all hemodynamic parameters were restricted to the acceleration phase of flow, with reduction in  $\theta_e$  significantly modifying the velocity gradient such that platelets tracking T14 were predicted to undergo a reduction in peak acceleration and  $\dot{\gamma}$ -gradient (Additional file 1: Fig. S3A & B); with more gradual velocity and  $\dot{\gamma}$  profiles (Fig. 3G, H). The  $\theta_e = 60^\circ$  geometry exhibited a  $\tau$  “inflection point” equivalent to that seen for  $\theta_e = 80^\circ$  (Fig. 3I). Significantly, transitioning from  $\theta_e = 60^\circ$  to  $40^\circ$  resulted in a complete loss of the  $\tau$  “inflection point,” with an order of magnitude increase in applied  $\tau$  proximal to acceleration start (Fig. 3I). In correlation with the observed shift in  $\tau$  profile as function of  $\theta_e$ , platelet  $[Ca^{2+}]_c$  flux across the acceleration phase was reduced for  $\theta_e = 20^\circ$  and  $40^\circ$ , with  $\theta_e = 20^\circ$  showing no significant  $[Ca^{2+}]_c$  flux over baseline controls (Fig. 3J, K). Overall,  $[Ca^{2+}]_c$  profiles increased directly with increasing  $\theta_e$  (Fig. 3K). Notably, there was no significant difference in  $[Ca^{2+}]_c$  maxima for  $\theta_e = 60^\circ$  and  $80^\circ$ , suggesting that the observed hemodynamic “inflection point” is a key driver of the signaling response (Fig. 3K).

To explore the downstream functional effects of  $[Ca^{2+}]_c$  flux as a function of acceleration profile, we developed a modified platelet aggregation assay (see “Methods”) in which the downstream face of the stenosis geometries were focally derivitized with purified human VWF (10  $\mu\text{g}/\text{mL}$ ), while all of the upstream components including the flow acceleration zone were blocked with 10%w/v bovine serum albumin (BSA) to prevent surface adhesion (Additional file 1: Fig. S1C &

D). This approach allowed for the acceleration-dependent platelet  $[Ca^{2+}]_c$  flux phase to be dissociated from possible GPIb/V/IX receptor engagement (Additional file 1: Fig. S1C & D). Significantly, using this approach, we demonstrate that downstream VWF-dependent platelet aggregation rate and extent directly correlate with acceleration profile ( $\theta_e$ ) in free flow, demonstrating that platelet mechanotransduction of flow acceleration has a direct and localized effect on platelet aggregation (Fig. 3L & Additional file 1: S3C).

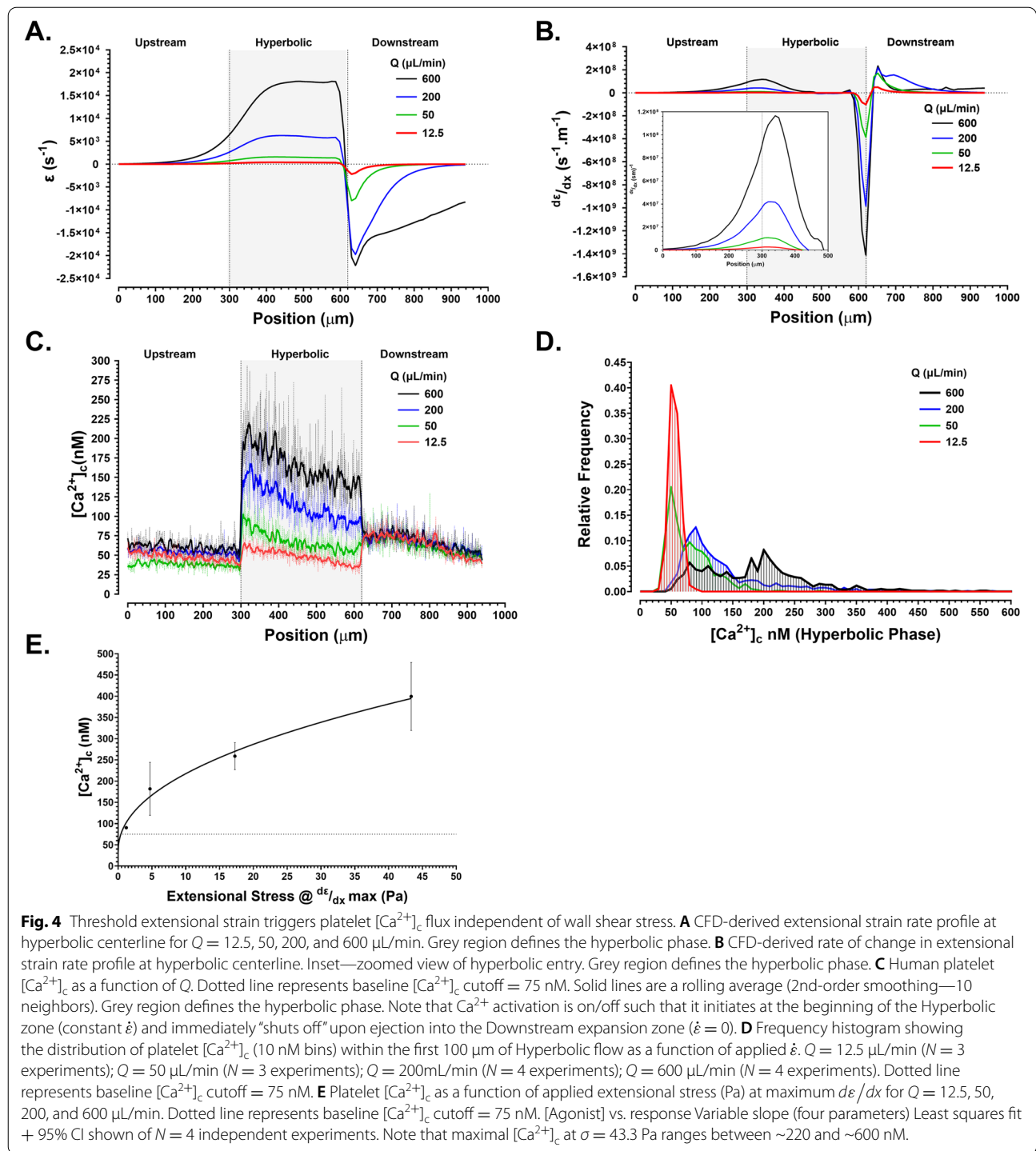
#### Extensional strain is the primary trigger of platelet $[Ca^{2+}]_c$ flux in the absence of adhesion receptor engagement

Having demonstrated that platelets in free flow (in the absence of adhesion receptor engagement) undergo significant and rapid  $[Ca^{2+}]_c$  flux in direct response to free-flow acceleration, we hypothesized that the extensional strain rate component of flow, through direct deformational effects on platelet structure, may be the key driver of this mechanotransduction mechanism. To test this hypothesis, we developed a hyperbolic microfluidic assay (see “Methods”) that subjects isolated human platelets to quasi-homogenous extensional strain rate (Cauchy strain rate,  $\dot{\epsilon}$ ) as a function of input flow rate ( $Q$ ) (Additional file 1: Fig. S4). The hyperbolic geometry was developed to generate peak  $\dot{\epsilon}$  (based on analytical solution) ranging between  $318 \text{ s}^{-1}$  ( $Q = 12.5 \mu\text{L}/\text{min}$ ) to  $>16,013 \text{ s}^{-1}$  ( $Q = 600 \mu\text{L}/\text{min}$ ) closely approximating the overall extensional strain component experienced in the stepped microfluidic geometries (Additional file 1: Fig. S2F). This approach allowed us to investigate the impact of  $\dot{\epsilon}$  in isolation from shear strain. Isolated human platelets resuspended in modified Tyrodes +  $\text{CaCl}_2$  (1 mM) buffer containing 0.5%w/v methylcellulose ( $\nu = 0.004 \pm 0.015 \text{ Pa}\cdot\text{s}$ ;  $\rho = 1016 \text{ kgm}^{-3}$ ) were perfused through this device at  $Q = 12.5, 50, 200,$  and  $600 \mu\text{L}/\text{min}$ . CFD modelling of centerline flow (corresponding to the platelet  $[Ca^{2+}]_c$  sampling region) through the hyperbolic microfluidic demonstrated that  $\dot{\epsilon}$  plateaued within  $100 \mu\text{m}$  of the hyperbolic throat at  $396 \text{ s}^{-1}$ ,  $1582 \text{ s}^{-1}$ ,  $6243 \text{ s}^{-1}$ , and  $18,118 \text{ s}^{-1}$  for  $Q = 12.5, 50, 200,$  and  $600 \mu\text{L}/\text{min}$  respectively (Fig. 4A). Platelets displayed a step-wise increase in  $[Ca^{2+}]_c$  flux as a function of  $Q$  and applied  $\dot{\epsilon}$ , with a significant right shift in the overall platelet  $[Ca^{2+}]_c$  frequency distribution (Fig. 4C, D). Peak platelet  $[Ca^{2+}]_c$  directly correlated with the maximal rate of change of  $\dot{\epsilon}$  ( $d\dot{\epsilon}/dx$ ) (Fig. 4B, C).  $[Ca^{2+}]_c$  flux was triggered at applied extensional stresses  $>1.2 \text{ Pa}$ , with maximal  $[Ca^{2+}]_c$  flux ranging between 314 and 560 nM at an applied extensional stress of  $43.3 \text{ Pa}$  ( $d\dot{\epsilon}/dx = 1.1 \times 10^8 \text{ s}^{-1} \text{ m}^{-1}$ ); approaching that seen with the  $\theta_e = 80^\circ$  acceleration geometry (Fig. 4E). Significantly,



$\dot{\varepsilon}$ -driven  $[Ca^{2+}]_c$  flux exhibited rapid On/Off behavior, such that ejection of the platelet sample into the downstream non-hyperbolic expansion resulted in immediate cessation of  $[Ca^{2+}]_c$  flux at  $d\varepsilon/dx \leq -3.0 \times 10^8 \text{ s}^{-1} \text{ m}^{-1}$  (Fig. 4A–C). Notably, platelet  $[Ca^{2+}]_c$  within the

hyperbolic zone exhibited a decline in magnitude over time of  $\sim 50\%$  that correlated with  $d\varepsilon/dx$  approaching  $0 \text{ s}^{-1} \text{ m}^{-1}$  (steadystate  $\dot{\varepsilon}$ ) (Fig. 4B, C), suggesting that this mechanotransduction process is rapidly downregulated once steadystate  $\dot{\varepsilon}$  is achieved.



This data supports our hypothesis that  $\dot{\epsilon}$  is a key hemodynamic driver of free-flow platelet  $Ca^{2+}$  flux and demonstrates that  $\dot{\epsilon}$  can trigger maximal platelet  $[Ca^{2+}]_c$  approaching  $600 \text{ nM}$ , in isolation from shear strain. We therefore define this platelet mechanotransduction phenomenon as “Extensional Strain Sensing ( $\dot{\epsilon}$ -S).”

**$\dot{\epsilon}$ -S is dependent on mechanically gated calcium influx**  
Having demonstrated a role for flow acceleration and  $\dot{\epsilon}$  in triggering platelet  $[Ca^{2+}]_c$  flux, we next explored the possible mechanism(s) of  $\dot{\epsilon}$ -S signal transduction. Initial experiments in the  $\theta_e = 80^\circ$  ( $Q = 200 \mu\text{L}/\text{min}$ ) geometry in which platelet activation was inhibited with  $PGE_1$

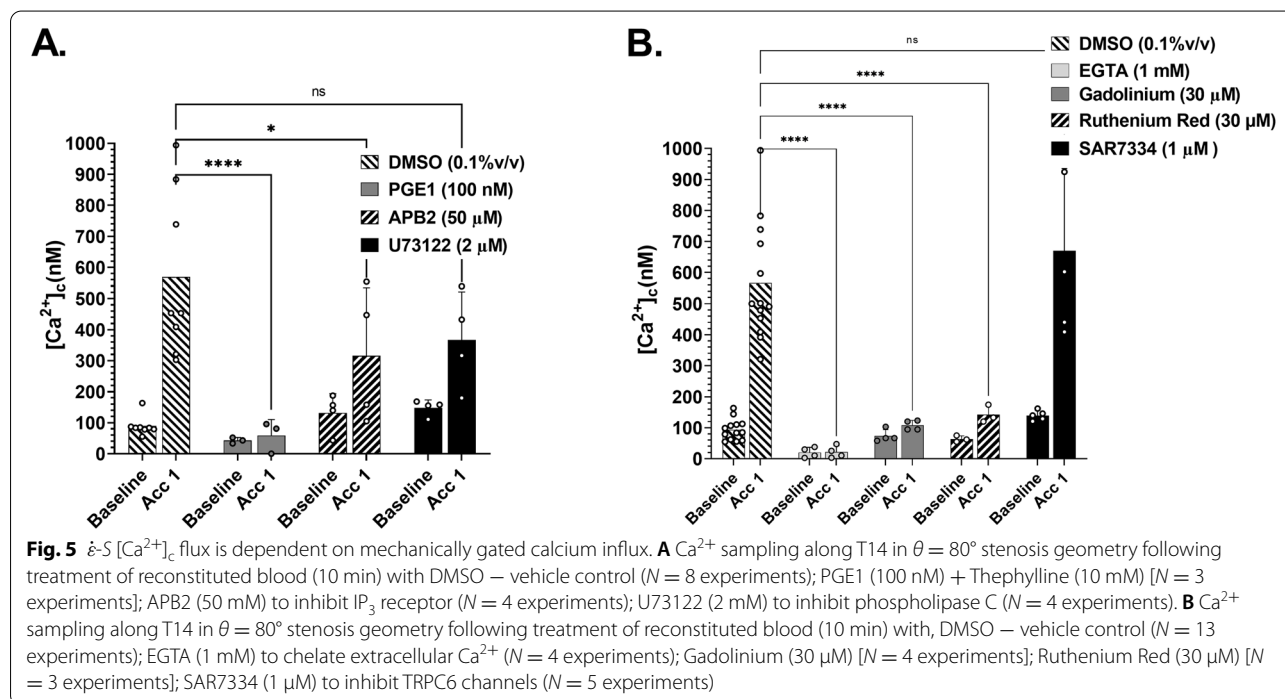
(100 nM) + Theophylline (10 mM) demonstrated that  $\dot{\epsilon}$ -S  $[Ca^{2+}]_c$  flux is an active signal transduction process and is regulated by intracellular [cAMP] (Fig. 5A). To investigate whether  $Ca^{2+}$  signaling was dependent on canonical  $IP_3$ -mediated store release, we treated reconstituted blood samples with U73122 (2  $\mu$ M) to inhibit  $IP_3$  generation by phospholipase C (PLC), or with the  $IP_3$  receptor blocker 2-Aminoethoxydiphenyl borate (APB2; 50  $\mu$ M) to inhibit store release. Figure 5A demonstrates that U73122 had no significant effect on  $\dot{\epsilon}$ -S  $[Ca^{2+}]_c$  flux, while APB2 had a minimal effect, suggesting that  $IP_3$ -mediated  $Ca^{2+}$  store release is not the major driver of  $\dot{\epsilon}$ -S signal transduction. We therefore hypothesized that  $\dot{\epsilon}$ -S  $[Ca^{2+}]_c$  flux is primarily driven by extracellular  $Ca^{2+}$  influx. To explore this, platelets + RBC were reconstituted in modified Tyrodes buffer in the presence of EGTA/ $Mg^{2+}$  (1 mM). Figure 5B demonstrates that chelation of extracellular  $Ca^{2+}$  completely suppressed baseline and  $\dot{\epsilon}$ -S  $[Ca^{2+}]_c$ , with  $[Ca^{2+}]_c = \sim 22$  nM; a  $\sim 78\%$  reduction compared to baseline controls. Given this dependency on extracellular  $Ca^{2+}$  influx, we posited that cationic mechanosensitive channels (MSCs) may be the primary driver(s) of  $\dot{\epsilon}$ -S  $[Ca^{2+}]_c$ . Figure 5B demonstrates that reconstituted blood samples treated with Gadolinium (30  $\mu$ M) or Ruthenium Red (30  $\mu$ M), to non-specifically block MSC-mediated  $Ca^{2+}$  influx, almost completely inhibited  $\dot{\epsilon}$ -S  $[Ca^{2+}]_c$  flux in response to flow acceleration ( $\theta_e = 80^\circ$ ). Inhibition of the SOCE-independent nonselective cation entry channel TRPC6 [19] with the selective antagonist SAR7334

(1  $\mu$ M) had no significant effect on  $\dot{\epsilon}$ -S  $[Ca^{2+}]_c$  (Fig. 5B). Taken together, these data suggest that  $\dot{\epsilon}$ -S signal transduction is mediated by an MSC-mediated process, independent of SOCE and TRPC6.

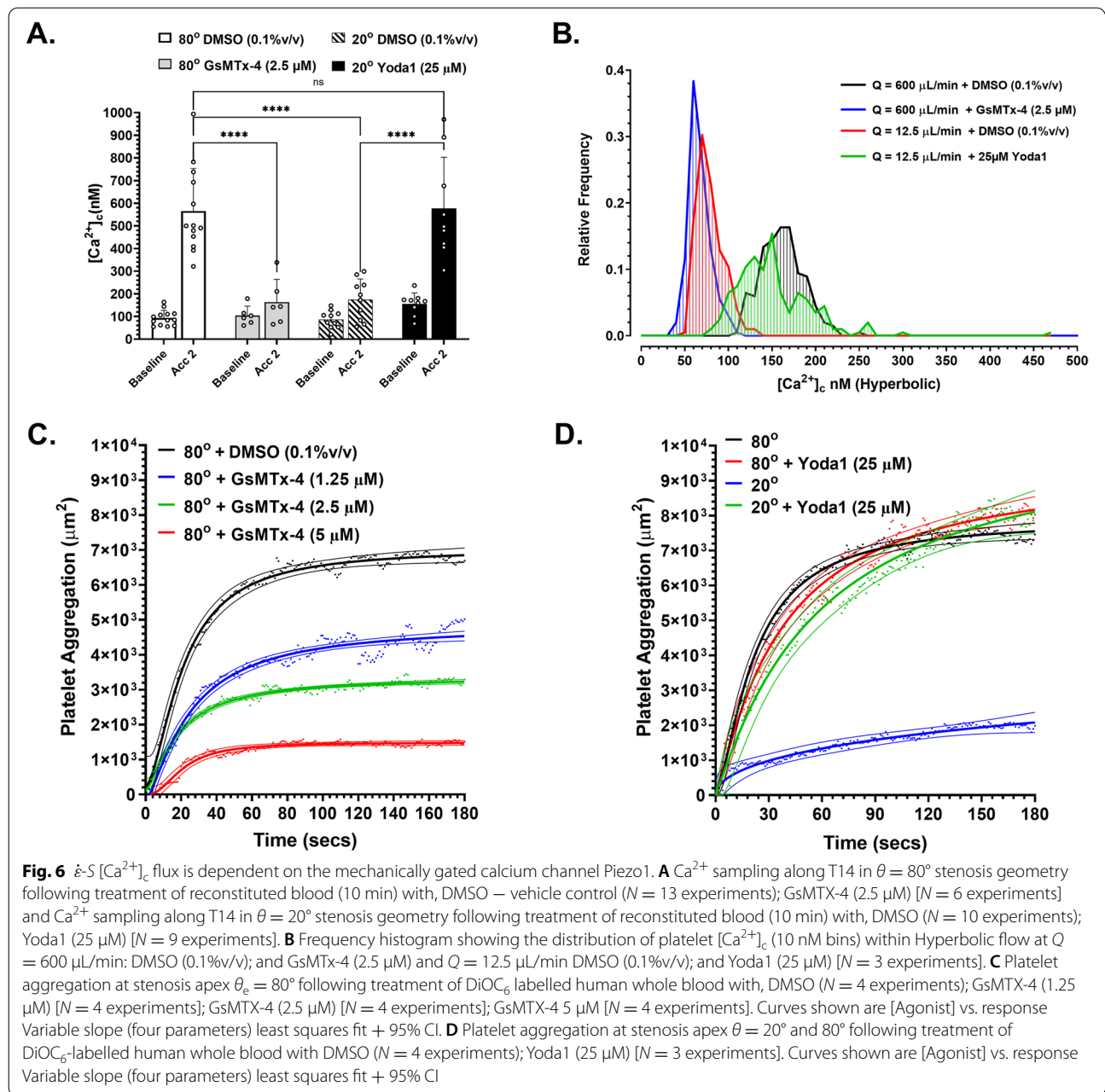
#### $\dot{\epsilon}$ -S is dependent on the mechanosensitive channel Piezo1

The platelet-expressed MSC, Piezo1, as a direct force sensor [20], has been implicated in shear-mediated platelet thrombus formation [21]. We therefore postulated that Piezo1 was acting as the primary MSC driving  $\dot{\epsilon}$ -S  $[Ca^{2+}]_c$  flux and as the direct  $\dot{\epsilon}$  sensor at free-flow acceleration. To investigate this, we conducted both stenosis-dependent and hyperbolic flow experiments in which reconstituted blood and isolated platelets respectively, were treated with the spider venom peptide *Grammos-tola spatulata* mechanotoxin 4 (GsMTx-4; Invitro Technologies); a non-specific MSC antagonist widely used to explore Piezo1 function [22]. Treatment of reconstituted blood with GsMTx-4 (2.5  $\mu$ M) 10 min prior to perfusion through the  $\theta_e = 80^\circ$  geometry ( $Q = 200$   $\mu$ L/min) significantly ( $P < 0.0001$ ) inhibited  $\dot{\epsilon}$ -S  $[Ca^{2+}]_c$  flux, with a  $\sim 88\%$  reduction in  $[Ca^{2+}]_c$  compared to control (Fig. 6A). In addition,  $\dot{\epsilon}$ -S  $[Ca^{2+}]_c$  flux at  $\dot{\epsilon} = 16,013$   $s^{-1}$  (hyperbolic flow) was completely inhibited by 2.5  $\mu$ M GsMTx-4 (Fig. 6B).

Given the lack of specificity of GsMTx-4 and to more definitively define a role for Piezo1 in mediating  $\dot{\epsilon}$ -S  $[Ca^{2+}]_c$  flux, we examined the capacity for the Piezo1-specific agonist Yoda1 (Sigma Aldrich) [23] to amplify  $\dot{\epsilon}$







-S signaling under subthreshold flow acceleration ( $\theta_e = 20^\circ$ ) and subthreshold  $\dot{\epsilon} = 197 \text{ s}^{-1}$ . Treatment of reconstituted blood with Yoda1 (25  $\mu$ M) at subthreshold acceleration resulted in a return of  $\dot{\epsilon}$ -S  $[Ca^{2+}]_c$  flux to that observed for  $\theta_e = 80^\circ$  controls, with  $[Ca^{2+}]_c \geq 600 \text{ nM}$  (Fig. 6A). In parallel, treatment of isolated platelets with Yoda1 (25  $\mu$ M) at a subthreshold  $\dot{\epsilon} = 318 \text{ s}^{-1}$  resulted in a return of  $\dot{\epsilon}$ -S  $[Ca^{2+}]_c$  flux (~79% increase) approaching that observed for  $\dot{\epsilon} = 16,013 \text{ s}^{-1}$  controls (Fig. 6B).

Finally, we explored the role of Piezo1 in mediating  $\dot{\epsilon}$ -S  $[Ca^{2+}]_c$  flux-affected platelet aggregation in

response to flow acceleration. Figure 6C demonstrates that GsMTx-4 can inhibit free-flow acceleration-mediated platelet aggregation in a concentration-dependent manner with 2.5  $\mu$ M GsMTx-4 resulting in a ~47% reduction and 5  $\mu$ M GsMTx-4 a ~76% reduction in endpoint aggregation at threshold acceleration ( $\theta_e = 80^\circ$ ). Conversely, treatment of whole blood with Yoda1 (25  $\mu$ M) under subthreshold acceleration ( $\theta_e = 20^\circ$ ) led to an ~8-fold increase in focal platelet aggregation, matching both aggregation rate and maxima of  $\theta_e = 80^\circ$  controls (Fig. 6D). Treatment of whole blood with

Yoda1 (25  $\mu\text{M}$ ) under maximal acceleration ( $\theta_e = 80^\circ$ ) led to no further increase over controls (Fig. 6D).

Taken together, these data demonstrate that Piezo1-mediated  $\text{Ca}^{2+}$  influx is a critical component of  $\dot{\epsilon}$ -S signal transduction and suggest that platelet Piezo1 is the primary force sensor facilitating adhesion-independent platelet  $\text{Ca}^{2+}$  activation in response to both blood flow acceleration and  $\dot{\epsilon}$ .

### $\dot{\epsilon}$ -S is critically dependent on concomitant ATP gated P2X1 $\text{Ca}^{2+}$ influx

Several studies have demonstrated a role for mechanical and chemical activation of Piezo1 in driving autocrine ATP release and subsequent purinergic receptor activation [24, 25]. In the case of platelets, autocrine release of

ATP and activation of the fast ATP-gated P2X1 cation channel has been demonstrated to be important for shear-mediated platelet activation and thrombus formation [26]. We therefore hypothesized that Piezo1 acts as the direct  $\dot{\epsilon}$  sensor and couples to P2X1 activation through local ATP release amplifying  $\dot{\epsilon}$ -S  $[\text{Ca}^{2+}]_c$  flux. To test this hypothesis, we assessed the effect of high [apyrase] (2 U/mL  $\geq 85\%$  ATPase; Sigma Aldrich) and direct inhibition of P2X1 with the highly specific antagonist NF449 (1  $\mu\text{M}$ ) [Merck] on flow acceleration ( $\theta_e = 80^\circ$ )-dependent  $\dot{\epsilon}$ -S  $[\text{Ca}^{2+}]_c$  flux. Figure 7A demonstrates that apyrase and NF449 led to a  $\sim 71\%$  and  $\sim 66\%$  reduction, respectively in  $\dot{\epsilon}$ -S  $[\text{Ca}^{2+}]_c$  flux. By extrapolation, in the absence of ATP/P2X1-dependent amplification, Piezo1 alone contributes  $\sim 29$  to  $35\%$  ( $\Delta[\text{Ca}^{2+}]_c = 101\text{--}138$  nM) of total  $\dot{\epsilon}$ -S  $[\text{Ca}^{2+}]_c$

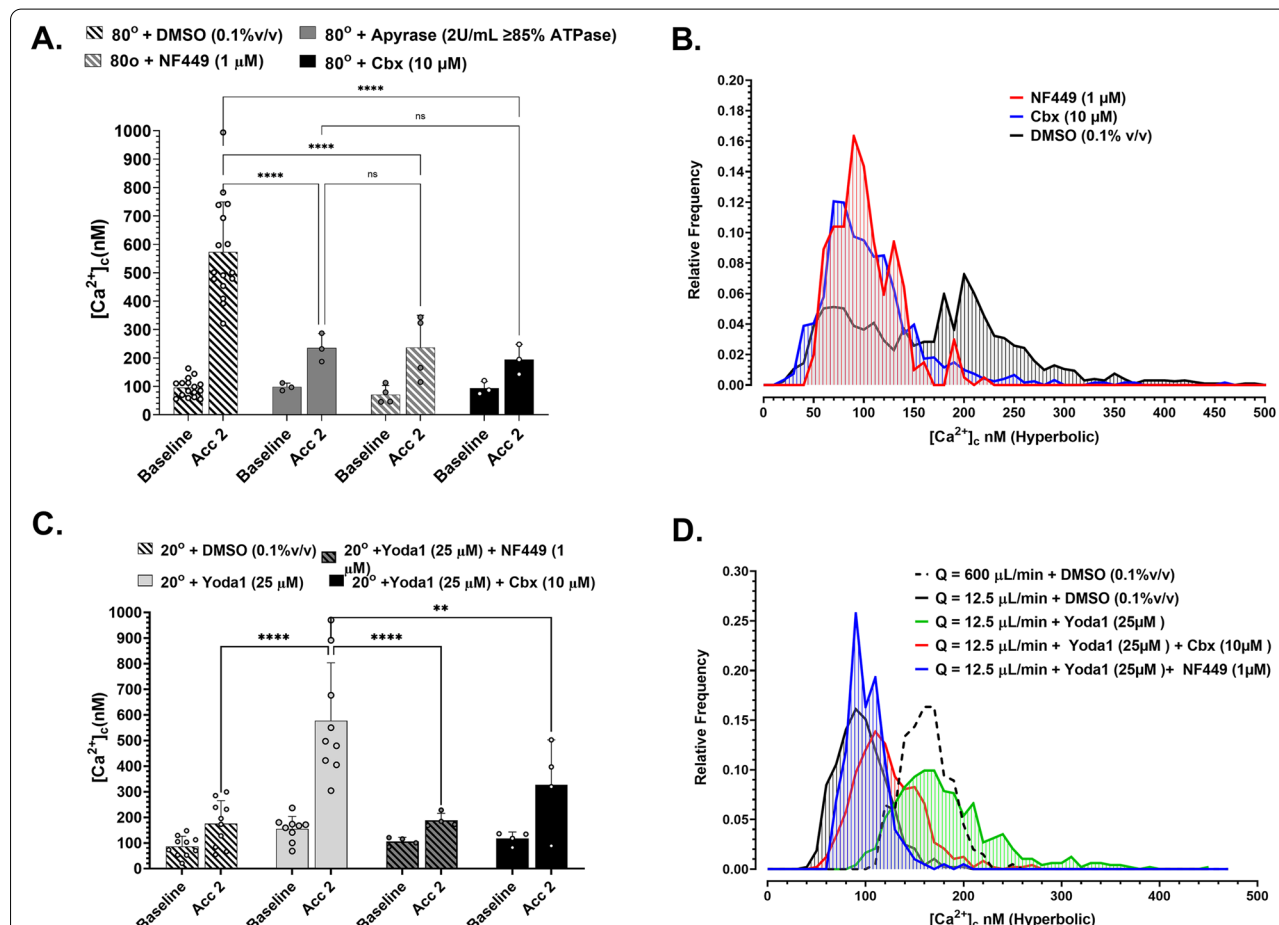


**Fig. 7**  $\dot{\epsilon}$ -S  $[\text{Ca}^{2+}]_c$  flux is dependent on Panx1 and P2X1. **A**  $\text{Ca}^{2+}$  sampling along T14 in  $\theta = 80^\circ$  stenosis geometry following treatment of reconstituted blood (10 min) with DMSO ( $N = 16$  experiments); Apyrase (2 U/mL  $\geq 85\%$  ATPase activity) [ $N = 3$  experiments]; NF449 (1  $\mu\text{M}$ ) [ $N = 4$  experiments]; Carbenoxolone (10  $\mu\text{M}$ ) [ $N = 3$  experiments]. **B** Frequency histogram showing the distribution of platelet  $[\text{Ca}^{2+}]_c$  (10 nM bins) within Hyperbolic flow at  $Q = 600$   $\mu\text{L}/\text{min}$ : DMSO (0.1% v/v); NF449 (1  $\mu\text{M}$ ); Carbenoxolone (Cbx; 10  $\mu\text{M}$ ) [ $N = 3$  independent experiments]. **C**  $\text{Ca}^{2+}$  sampling along T14 in  $\theta = 20^\circ$  stenosis geometry following treatment of reconstituted blood (10 min) with DMSO ( $N = 10$  experiments); Yoda1 (25  $\mu\text{M}$ ) [ $N = 9$  experiments]; Yoda1 (25  $\mu\text{M}$ ) + Cbx (10  $\mu\text{M}$ ) [ $N = 3$  experiments]; Yoda1 (25  $\mu\text{M}$ ) + NF449 (1  $\mu\text{M}$ ) [ $N = 4$  experiments]. **D** Frequency histogram showing the distribution of platelet  $[\text{Ca}^{2+}]_c$  (10 nM bins) within Hyperbolic flow at  $Q = 600$   $\mu\text{L}/\text{min}$

flux under the conditions tested. Platelet aggregation at flow acceleration ( $\theta_e = 80^\circ$ ) showed a  $\sim 30\%$  reduction in endpoint aggregate size in the presence of NF449 (1  $\mu\text{M}$ ) (Fig. S5). Hyperbolic flow experiments demonstrated that at  $\dot{\epsilon} = 16,013 \text{ s}^{-1}$ ,  $\dot{\epsilon}\text{-S } [\text{Ca}^{2+}]_c$  flux was almost completely inhibited by NF449 (1  $\mu\text{M}$ ) (Fig. 7B).

Based on these data and published data describing a role for the ATP permeable hemichannel pannexin1 (Pannx1) in mediating platelet ATP release,  $\text{Ca}^{2+}$  influx, platelet aggregation, and thrombus formation [27], we examined the effect of the Pannx1 inhibitor carbenoxalone (Cbx; 10  $\mu\text{M}$ ) in modulating  $\dot{\epsilon}\text{-S } [\text{Ca}^{2+}]_c$  flux. Figure 7A and B demonstrate that Cbx (10  $\mu\text{M}$ ) lead to an  $\sim 80\%$  reduction in  $\dot{\epsilon}\text{-S } [\text{Ca}^{2+}]_c$  flux equivalent to that observed for apyrase and NF449 treatment. Cbx (10  $\mu\text{M}$ ) also inhibited platelet aggregation at ( $\theta_e = 80^\circ$ ) flow acceleration and was typified by observable cyclic embolization indicative of unstable platelet aggregation (Additional file 1: Fig. S5).

Finally, to explore the interaction between Piezo1 gating and ATP-P2X1 mediated  $\dot{\epsilon}\text{-S } [\text{Ca}^{2+}]_c$  flux, we conducted a series of combinatorial experiments under subthreshold flow acceleration ( $\theta_e = 20^\circ$ ) and subthreshold  $\dot{\epsilon} = 318 \text{ s}^{-1}$  in which reconstituted blood or isolated platelets respectively were treated with Yoda1 (25  $\mu\text{M}$ ) to potentiate Piezo1 gating in combination with NF449 (1  $\mu\text{M}$ ) or Cbx (10  $\mu\text{M}$ ). Figure 7C and D demonstrate that under these subthreshold conditions Yoda1 (25  $\mu\text{M}$ ) mediated restoration of  $\dot{\epsilon}\text{-S } [\text{Ca}^{2+}]_c$  flux was inhibited by  $\sim 80\%$  in the presence of NF449 (1  $\mu\text{M}$ ) and  $\sim 51\%$  by Cbx (10  $\mu\text{M}$ ). Taken together, these data demonstrate that  $\dot{\epsilon}\text{-S } [\text{Ca}^{2+}]_c$  flux is mediated by mechanical activation of Piezo1 in response to  $\dot{\epsilon}$  leading to downstream gating of Pannx1 and localized release of ATP, triggering subsequent P2X1 gating and  $\text{Ca}^{2+}$  influx. Overall, these data suggest that P2X1 plays a significant role in amplifying  $[\text{Ca}^{2+}]_c$  influx initially triggered by Piezo1 mechanosensing.

### Type II PI3 kinase C2 $\alpha$ activity critically modulates $\dot{\epsilon}\text{-S}$

Using both inducible knockdowns in mice and first in class inhibitors of the type II PI3 kinase (PI3K) C2 $\alpha$

isoform, we have previously demonstrated that velocity gradient-dependent platelet aggregation is significantly dependent on PI3KC2 $\alpha$  activity [28, 29]. In addition, modelling studies have suggested a role for membrane lipid composition and in particular phosphoinositides in modulating Piezo1 conformation and gating [30]. We therefore hypothesized that PI3K isoforms and specifically PI3K C2 $\alpha$  may be a key modulator of  $\dot{\epsilon}\text{-S}$  signal transduction. To test this hypothesis, we conducted a broad screen of PI3K inhibitors and assessed their effect following perfusion of reconstituted blood through the  $\theta_e = 80^\circ$  geometry. Figure 8A demonstrates that neither Copanlisib (10  $\mu\text{M}$ ) [Sigma Aldrich] nor Wortmannin (100 nM) [Sigma Aldrich], as pan-specific PI3K inhibitors, showed significant inhibition of  $\dot{\epsilon}\text{-S } [\text{Ca}^{2+}]_c$  flux. Equally, neither the Type I PI3K $\gamma$  inhibitor AS252424 (2  $\mu\text{M}$ ) [Sigma Aldrich] nor the PI3K $\beta$  inhibitor TGX221 (0.5  $\mu\text{M}$ ) [Sigma Aldrich] had significant effect on  $\dot{\epsilon}\text{-S } [\text{Ca}^{2+}]_c$  flux (Fig. 8A). In contrast, the PI3K C2 $\alpha$ -specific inhibitor MIPS-21335 (10  $\mu\text{M}$ ) [29] completely inhibited  $\dot{\epsilon}\text{-S } [\text{Ca}^{2+}]_c$  flux with an  $\sim 88\%$  reduction in  $[\text{Ca}^{2+}]_c$ , while its inactive analog CM-851-106A (10  $\mu\text{M}$ ) showed no inhibitory effect (Fig. 8A). Parallel investigation of the inhibitory effect of MIPS-21335 on isolated platelets as a function of  $\dot{\epsilon} = 16,013 \text{ s}^{-1}$  supported this finding, demonstrating a significant role for PI3K C2 $\alpha$  in modulating  $\dot{\epsilon}\text{-S } [\text{Ca}^{2+}]_c$  flux (Fig. 8B). In corroboration of our prior published studies [29], inhibition of PI3K C2 $\alpha$  with MIPS-21335 significantly attenuated acceleration-dependent platelet aggregation with a  $\sim 50\%$  reduction in endpoint aggregate size and an observable reduction in the initial rate of platelet aggregation at the  $\theta_e = 80^\circ$  stenosis geometry (Fig. 8C). In contrast, potentiation of Piezo1-mediated  $[\text{Ca}^{2+}]_c$  influx with Yoda1 (25  $\mu\text{M}$ ) at subthreshold acceleration ( $\theta_e = 20^\circ$ ) was not effected by MIPS-21335 (10  $\mu\text{M}$ ), suggesting that direct modulation of Piezo1 by Yoda1 uncouples the requirement for PI3K C2 $\alpha$  activity and by extrapolation that PI3K C2 $\alpha$  sits sequentially upstream of Piezo1 gating (Fig. 8D).

Finally, heterozygous inactivation of PI3K C2 $\alpha$  in mice has been demonstrated to lead to defects in platelet

(See figure on next page.)

**Fig. 8** Type II PI3 kinase C2 $\alpha$  activity modulates  $\dot{\epsilon}\text{-S } [\text{Ca}^{2+}]_c$  flux. **A**  $\text{Ca}^{2+}$  sampling along T14 in  $\theta = 80^\circ$  stenosis geometry following treatment of reconstituted blood (10 min) with DMSO (0.1%v/v) [ $N = 8$  experiments]; Copanlisib (10  $\mu\text{M}$ ) [ $N = 3$  experiments]; Wortmannin (100 nM) [ $N = 3$  experiments]; AS252424 (2  $\mu\text{M}$ ) [ $N = 3$  experiments]; TGX221 (0.5  $\mu\text{M}$ ) [ $N = 3$  experiments]; MIPS-21335 (10  $\mu\text{M}$ ) [ $N = 4$  experiments]; CM-851-106A (10  $\mu\text{M}$ ) [ $N = 4$  experiments]. **B** Frequency histogram showing the overall distribution of platelet  $[\text{Ca}^{2+}]_c$  (10 nM bins) within Hyperbolic flow at  $Q = 600 \mu\text{L}/\text{min}$ : DMSO (0.1%v/v); MIPS-21335 (10  $\mu\text{M}$ ); CM-851-106A (10  $\mu\text{M}$ ). **C** Platelet aggregation at stenosis apex  $\theta = 80^\circ$  following treatment of DiOC $_6$  labelled human whole blood with, DMSO (0.1%v/v) [ $N = 6$  experiments]; MIPS-21335 (10  $\mu\text{M}$ ) [ $N = 6$  experiments]; MIPS-21335 (1  $\mu\text{M}$ ) [ $N = 3$  experiments]; CM-851-106A (10  $\mu\text{M}$ ) [ $N = 4$  experiments]. Curves shown are [Agonist] vs. response Variable slope (four parameters) least squares fit + 95% CI. **D**  $\text{Ca}^{2+}$  sampling along T14 in  $\theta = 20^\circ$  stenosis geometry following treatment of reconstituted blood (10 min) with DMSO (0.1%v/v) [ $N = 10$  experiments]; Yoda1 (25  $\mu\text{M}$ ) [ $N = 9$  experiments]; Yoda1 (25  $\mu\text{M}$ ) + MIPS-21335 (10  $\mu\text{M}$ ) [ $N = 3$  experiments]. **E**  $\text{Ca}^{2+}$  sampling along T14 in  $\theta_e = 80^\circ$  stenosis geometry following treatment of reconstituted blood (10 min) with DMSO (0.1%v/v) [ $N = 3$  experiments]; Latrunculin B (8  $\mu\text{M}$ ) [ $N = 3$  experiments]; Jaspilakinolide (5  $\mu\text{M}$ ) [ $N = 3$  experiments]; Blebbistatin (10  $\mu\text{M}$ ) [ $N = 3$  experiments]; Cytochalasin D (5  $\mu\text{M}$ ) [ $N = 3$  experiments]

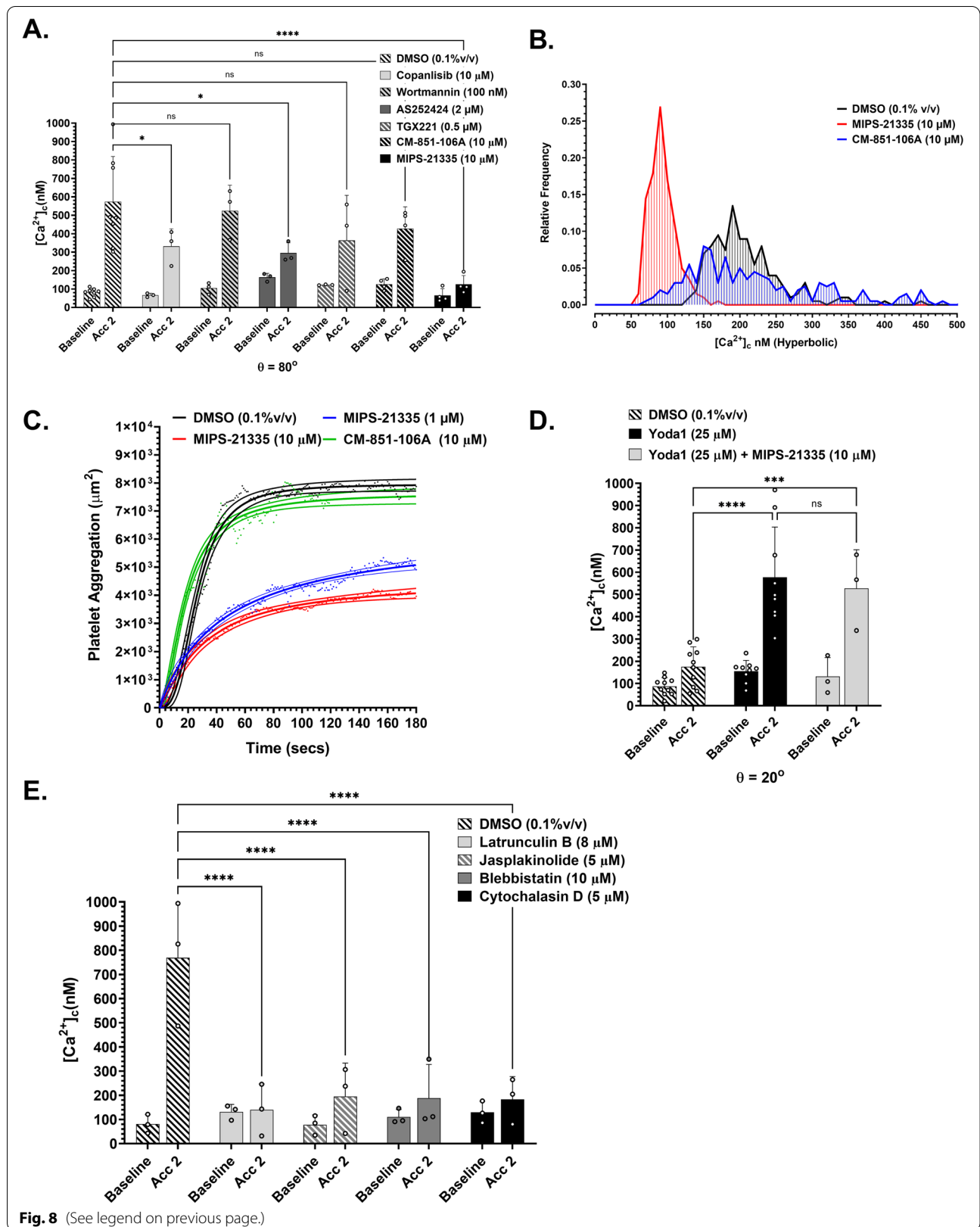


**Fig. 8** (See legend on previous page.)

thrombus formation with concomitant rigidification of the platelet plasma membrane and associated mislocation of several membrane cytoskeletal proteins [31]. We therefore posited that coupling of  $\dot{\epsilon}$  to  $\dot{\epsilon}$ -S  $[Ca^{2+}]_c$  flux is modulated by PI3K C2 $\alpha$ -dependent cytoskeletal dynamics and associated membrane mechanics. As a preliminary test of this hypothesis, we ran a panel of pharmacological cytoskeletal inhibitors under conditions of threshold acceleration ( $\theta = 80^\circ$ ). Figure 8E demonstrates that  $\dot{\epsilon}$ -S  $[Ca^{2+}]_c$  flux is critically dependent on active cytoskeletal dynamics such that inhibition of cytoskeletal polymerization (Cytochalasin D; 5  $\mu$ M or Latrunculin B; 8  $\mu$ M; Sigma Aldrich), disordering of polymeric actin (Jasplakinolide; 5  $\mu$ M; Sigma Aldrich), or inhibition of myosin II activity (Blebbistatin; 10  $\mu$ M; Sigma Aldrich) completely inhibited  $\dot{\epsilon}$ -S signal transduction. Taken together, these data demonstrate that PI3K C2 $\alpha$  plays a critical role in regulating  $\dot{\epsilon}$ -S and by extrapolation suggests that membrane PI(3)P and membrane/cytoskeletal mechanics play a significant modulatory role coupling  $\dot{\epsilon}$  to platelet Piezo1 mechanosensing in free flow.

## Discussion

A large volume of work has explored the role of platelet adhesion receptors in mechanotransducing the external forces of blood flow, with wall shear rate/stress and compressive forces given specific attention [5, 6, 13]. These studies have led to an overall model of platelet activation under steady-state shear whereby initial platelet engagement with shear-decryptated VWF, either free in plasma, expressed at the endothelial surface, or adhered to exposed extracellular collagen, leads to initial GPIb/V/IX-mediated mechanotransduction and subsequent integrin  $\alpha_{IIb}\beta_3$  outside-in signaling. Key to these mechanosensing processes are the effects of tensile and compressive forces on adhesion receptor conformation, and transmission of force to integral membrane proteins and the underlying cytoskeleton. While critical to overall platelet function and thrombus formation, this model does not consider the effects of blood flow hemodynamics on platelet activation and function in free flow. Here, we report for the first time (to our knowledge) that in the absence of canonical adhesion receptor engagement, VWF binding, and platelet amplification loops, platelets are capable of directly mechanosensing suprphysiological changes in blood flow acceleration and more specifically extensional strain rate ( $\dot{\epsilon}$ ). Significantly, we demonstrate that platelet activation occurs in response to  $\dot{\epsilon}$  rather than peak shear stress magnitude. Using a pharmacological approach, we define an “Extensional Strain Sensing ( $\dot{\epsilon}$ -S) mechanosome” comprised of three primary subunits: a principal mechanosensor in the form of membrane-localized Piezo1, a coupled  $Ca^{2+}$  signal amplifier in the form of the

fast ATP-gated cation channel P2X1, and a modulatory “clutch” comprised of the type II PI3 kinase C2 $\alpha$  isoform (Fig. 9). Our findings have significant implications for our understanding of platelet function and thrombosis under pathological or device-induced suprphysiological hemodynamics, establishing that hemodynamic parameters in isolation, and specifically  $\dot{\epsilon}$ , are sufficient to trigger platelet activation.

Regarding the  $\dot{\epsilon}$ -S mechanosome, our pharmacological data support a key role for Piezo1 as the primary mechanosensor (Fig. 9) triggering  $\dot{\epsilon}$ -S  $[Ca^{2+}]_c$  flux under conditions of both free-flow trajectory-dependent acceleration and quasi-homogenous  $\dot{\epsilon}$ . This finding is underpinned by transcriptomic and proteomic data demonstrating Piezo1 expression in human platelets [32, 33] and findings that platelet  $Ca^{2+}$  entry stimulated by physiological  $\dot{\gamma}$  in the range of 1003–3989  $s^{-1}$ , is sensitive to both GsMTx-4 inhibition and Yoda1 potentiation [21]. Our data demonstrate that inhibition of Piezo1 with GsMTx-4 leads to effective inhibition of  $\dot{\epsilon}$ -S  $[Ca^{2+}]_c$  flux and a correlated inhibition of downstream functional platelet aggregation. Significantly, under subthreshold flow acceleration and  $\dot{\epsilon}$  (at which  $\dot{\epsilon}$ -S  $[Ca^{2+}]_c$  flux and aggregation were minimal), the Piezo1 agonist Yoda1 potentiated  $[Ca^{2+}]_c$  flux and associated aggregation comparable to high acceleration and  $\dot{\epsilon}$ -controls. These findings are supported by studies showing that Yoda1 predominantly affects Piezo1 sensitivity and inactivation kinetics in response to mechanical stimulation, whereby Yoda1 acts as a “molecular wedge” amplifying force-induced Piezo1 conformational changes; lowering the channel threshold for activation [24, 34]. While our findings support prior studies for a role of Piezo1 in platelet function, there are some key differences: (i) Ilkan et al. [21] describe a set of experimental conditions in which human platelets were first surface-immobilized via an anti-PECAM1 antibody prior to  $\dot{\gamma}$  exposure and thus were unable to differentiate between surface-derived tensile stresses and direct effects of applied  $\dot{\gamma}$ . Furthermore, their study could not exclude inputs from morphological changes and associated signaling induced by surface adhesion [21]. In contrast, our studies define a role for Piezo1 in the direct mechanosensing of applied  $\dot{\epsilon}$  in the complete absence of surface adhesion and shear strain; (ii) Ilkan et al. [21] also describe the effects of steady-state (4-min duration) physiological  $\dot{\gamma}$  that trigger stochastic  $[Ca^{2+}]_c$  transients exhibiting significant lagtimes of  $\sim 1$  min post-shear initiation [21]. In contrast, our data demonstrate that under non-steady-state suprphysiological  $\dot{\gamma}$  gradients and quasi-homogenous  $\dot{\epsilon}$  conditions that Piezo1-mediated  $[Ca^{2+}]_c$  flux occurs immediately upon  $\dot{\epsilon}$  exposure. These prior studies in combination with our own suggest that free-flow mediated effects on platelet Piezo1 gating may

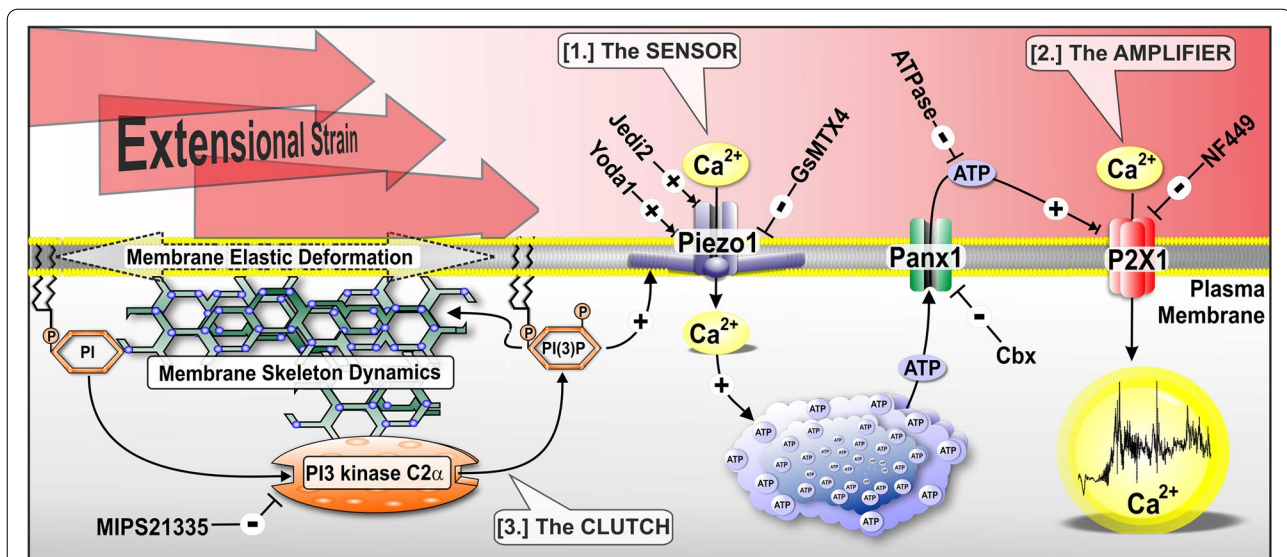


**Fig. 9** Working model of the Extensional Strain Sensing ( $\epsilon$ -S) Mechanosome. Extensional strain ( $\epsilon$ ) generated by flow acceleration and acute changes in platelet trajectory impose a deformational load on the platelet plasma membrane and underlying spectrin-based membrane skeleton engaging the  $\epsilon$ -S mechanosome comprised of [1.] *The Sensor*—Piezo1 gating driven by deformational stress loading of the plasma membrane and membrane skeleton (membrane tension) leads to low level  $\text{Ca}^{2+}$  influx; [2.] *The Amplifier*—Piezo1-mediated  $\text{Ca}^{2+}$  influx triggers near-membrane ATP release via Pannexin1 (Panx1) triggering subsequent P2X1 activation, amplifying  $\epsilon$ -S  $[\text{Ca}^{2+}]_i$  flux; [3.] *The Clutch*—A localized pool of PI(3)P, dependent on basal PI3-kinase C2 $\alpha$  activity, modulates membrane skeleton composition, membrane elastic deformation, and associated force coupling through the plasma membrane to Piezo1

be further modulated by adhesion-dependent signaling and that platelet Piezo1 may require significantly higher threshold  $\dot{\gamma}$ , in the absence of surface adhesions, to trigger  $\text{Ca}^{2+}$  influx.

Our data support a role for ATP release via the Panx1 hemichannel and associated P2X1-mediated  $\text{Ca}^{2+}$  influx in  $\epsilon$ -S. Significantly, our data suggest that in the absence of ATP-P2X1 signaling that Piezo1 alone contributes only ~29–35% of total  $\text{Ca}^{2+}$  influx, indicating that P2X1 plays a major role in amplifying  $\epsilon$ -S  $[\text{Ca}^{2+}]_i$ . We demonstrate that blockade of P2X1 activation with the specific antagonist NF449 reduced endpoint aggregation in our system by ~30%, while concentration-dependent GsMTx-4 inhibition led to a 47–76% reduction in aggregate size. This apparent dichotomy between the contributions of P2X1 and Piezo1 to  $\text{Ca}^{2+}$  flux magnitude versus aggregation dynamics may indicate that receptor-mediated outside-in and soluble agonist signaling following platelet recruitment to the developing aggregate reduce the requirement for P2X1 amplification and in turn modify the contribution by Piezo1. Furthermore, once surface or platelet-platelet adhesions have been established, the effects of local hemodynamics on deformational stress loading of the platelet plasma membrane and underlying membrane skeleton are likely to be substantially different, with both compressive and tensile loading of adhesion receptors and platelet structures contributing to ongoing platelet

$\text{Ca}^{2+}$  flux. These findings demonstrating co-dependency between Piezo1 and P2X1 signaling in  $\epsilon$ -S are supported by accumulating evidence for a role for ATP release and P2 receptor signaling in mediating Piezo1-dependent mechanoregulation in a number of cell types, including vascular endothelial cells, and red blood cells [24, 25, 35, 36]. Notably, these prior studies using both pharmacologic and siRNA suppression strategies have shown a key role for the Panx1 hemichannel as the primary mediator of Piezo1-triggered ATP release at threshold shear stresses >3 Pa [35, 36].

There is accumulating evidence showing that membrane lipids have both positive and negative modulatory effects on Piezo1 function, with these effects likely due to alterations in global membrane properties such as bending rigidity or stiffness of the local lipid bilayer [30, 37, 38]. Specifically, molecular dynamics simulations of Piezo1 in complex lipid bilayers have implicated a role for membrane phosphoinositide phosphates (PIPs) in modulating Piezo1 conformation and gating [30]. These studies predict that negative lipid species including PI(3)P share common binding sites proximal to the Piezo1 cation channel pore [30]. Our data, for the first time (to our knowledge), demonstrate that type II PI3K C2 $\alpha$  activity and by corollary PI3K C2 $\alpha$ -generated lipids are critical mediators of  $\epsilon$ -S and by extrapolation Piezo1-mediated mechanosensing. Our findings are

underpinned by previously published data from our laboratories demonstrating that platelet aggregation under moderate  $\dot{\gamma}$  conditions ( $\dot{\gamma} = 1800\text{--}22,500\text{ s}^{-1}$ ) was suppressed by both pharmacologic inhibition and inducible depletion of PI3KC2 $\alpha$  [28, 29]. Significantly, these prior studies demonstrated that pharmacologic inhibition with the PI3KC2 $\alpha$ -specific inhibitor MIPS-21335 reduced endpoint platelet aggregation (with and without platelet amplification loop blockade) approaching  $\sim 55\%$  [29], matching the inhibitory effect in the present study ( $\sim 50\%$  reduction) under significantly more acute  $\dot{\gamma}$  conditions ( $\dot{\gamma} = 100\text{--}100,000\text{ s}^{-1}$ ). Given that we show that upstream  $\dot{\epsilon}$ -S  $[\text{Ca}^{2+}]_c$  flux and correlated downstream platelet aggregation scale with acceleration magnitude and Q (Fig. 3H & S2C), the equivalency of MIPS-21335 inhibition at moderate [28, 29] and suprphysiological hemodynamic gradients (Fig. 1A) suggests that PI3KC2 $\alpha$  activity is absolutely required for  $\dot{\epsilon}$ -S.

We demonstrate that  $\dot{\epsilon}$ -S signaling is not affected by the pan-specific PI3K inhibitor Wortmannin, the pan-class I inhibitor Copanlisib, nor the type I isoform-specific PI3K inhibitors AS2524424 and TGX221, directed against PI3K $\gamma$  and PI3K $\beta$  respectively; supporting a specific role for the type II PI3KC2 $\alpha$  isoform. The apparent lack of effect of Wortmannin may be attributed in part to its overall lack of specificity for PI3K C2 $\alpha$ , with an approximate  $\text{IC}_{50}$  for PI3K C2 $\alpha$  of 400 nM [39], four times the concentration used in the present study. Notably, we demonstrate that potentiation of Piezo1 with Yoda1 completely abrogated the effect of specific PI3K C2 $\alpha$  inhibition, suggesting that reduction in the mechanical threshold for Piezo1 activation by Yoda1 eliminates the requirement for PI3K C2 $\alpha$  generated lipid species. Given the “molecular wedge” hypothesis of Yoda1 action [23, 34] and findings that strong protein-lipid interactions are required to anchor the bilayer around the curved shape of Piezo1 [40], alterations in local membrane curvature by Yoda1 may limit the requirement for PI3K C2 $\alpha$ -derived PIPs.

Whereas class I PI3Ks reside mainly in the cytoplasm until recruited to active signaling complexes, the class II PI3Ks are largely constitutively associated with membrane structures and produce both PI(3)P and PI(3,4)P2 species. Recent data suggests that platelet PI3K C2 $\alpha$  controls a basal pool of PI(3)P with slow turnover rate that is not involved in agonist-induced PI(3)P generation or a major change in overall lipid composition [31]. These prior studies demonstrate that inactivation of platelet PI3K C2 $\alpha$  results in a change in the composition of the spectrin-based-membrane skeleton, with measurable reductions in spectrin, myosin, filamin, moesin, GPIb $\alpha$ , and GPIIb content [31]. These changes in membrane skeleton composition were associated with an overall

increase in plasma membrane rigidity and correlated defects in platelet thrombosis [31]. Our preliminary pharmacological data demonstrate that acto-myosin-based cytoskeletal dynamics are a key player in  $\dot{\epsilon}$ -S, with inhibition of actin polymerization, turnover, and contractile function all leading to complete inhibition of  $\dot{\epsilon}$ -S  $[\text{Ca}^{2+}]_c$  flux. Taken together with the almost complete blockade of  $\dot{\epsilon}$ -S  $[\text{Ca}^{2+}]_c$  flux with MIPS-21335, these data point toward a mechanism whereby basal PI3K C2 $\alpha$  activity and associated membrane [PI(3)P], in concert with membrane skeleton composition and dynamics, play a critical role in “coupling” externally applied  $\dot{\epsilon}$  to the  $\dot{\epsilon}$ -S mechanosome and more specifically Piezo1 (Fig. 9). These findings track with the involvement of membrane bending rigidity or stiffness in modulating Piezo1 mechanosensing. A full delineation of the interplay between the membrane skeleton, PI3K C2 $\alpha$  lipid products, and membrane dynamics while outside the scope of the current study is a subject for future investigation.

By mapping the precise temporal progression of platelet  $\text{Ca}^{2+}$  signaling to individual platelet trajectories in blood flow at idealized stenoses, we demonstrate that platelets exhibit distinct streamline-dependent  $\text{Ca}^{2+}$  signal activation statuses contingent on their acceleration profile. Critically, our data demonstrate that rather than responding to peak steadystate  $\tau$ , platelet activation is initially triggered by very early transitions in free-flow strain at the very start of flow acceleration. Our experiments using isolated platelet preparations exposed to quasi-homogenous  $\dot{\epsilon}$  critically support this finding and demonstrate that platelet activation is attuned to the rate of change in  $\dot{\epsilon}$  application and On/Off in nature, such that  $\dot{\epsilon}$ -S  $[\text{Ca}^{2+}]_c$  flux shuts down upon immediate cessation of  $\dot{\epsilon}$ . These findings track with our observations that platelet  $[\text{Ca}^{2+}]_c$  flux at stenosis downregulates across the acceleration phase and continues to downregulate post-stenosis returning to baseline levels. This short-range effect suggests that the  $\dot{\epsilon}$ -S mechanosome is triggered by acute changes in membrane and cytoskeletal elastic deformations and/or rapid changes in membrane tension that become quiescent once steadystate  $\dot{\epsilon}$  is achieved. This concept is supported by our  $\dot{\epsilon}$  experiments where overall  $\dot{\epsilon}$ -S  $[\text{Ca}^{2+}]_c$  flux reduced by 50% when the rate of change in  $\dot{\epsilon}$  approached zero. While structural accommodations of the plasma membrane and underlying spectrin-based-membrane skeleton to the applied steadystate  $\dot{\epsilon}$  may in part explain this refractory behavior, voltage-dependent inactivation and desensitization of Piezo1 [41] and rapid desensitization of P2X1 [42] may also contribute to the observed decay of  $\dot{\epsilon}$ -S  $[\text{Ca}^{2+}]_c$  flux.

Early studies by Strony et al. [7] using experimental Folts and CFD models to correlate hemodynamics and platelet thrombosis raised the possibility that  $\dot{\epsilon}$  and

elongational platelet deformation at stenosis entry are important in promoting thrombus formation. However, very few follow-up studies have investigated the impact of  $\dot{\epsilon}$  regimes on platelet activation. Based on computational modelling of a defined 84% axisymmetric arterial stenosis (in which the contraction and expansion in flow geometry followed a sinusoidal function), Bluestein et al. proposed that elongation stresses produced by convective acceleration at arterial contraction may play a role in platelet activation [43]. They reported that  $\dot{\epsilon}$ , computed along a select near wall trajectory, reached values of up to  $600 \text{ s}^{-1}$  (at  $\text{Re} = 3600$ ) [43]. These modelling data fall well within the range of the present study where we demonstrate that free-flow platelet activation can occur at an  $\dot{\epsilon} \geq 747 \text{ s}^{-1}$ . In the case of the microcirculation, changes in vessel radius of  $\sim 20\%$ , at a typical pre-constriction blood velocity of  $\sim 0.1 \text{ m/s}$ , have been shown to generate  $\dot{\epsilon}$  of  $\sim 5 \times 10^3 \text{ s}^{-1}$  [44]. Extensional strain of this magnitude, known to trigger unfolding of VWF and subsequent platelet adhesion, sits well within the midrange of our hyperbolic microfluidic studies ( $Q = 200 \mu\text{L}/\text{min}$ ) which we show trigger significant adhesion-independent platelet  $[\text{Ca}^{2+}]_c$  activation. In this context,  $\dot{\epsilon}$  regimes of the order of those utilized in this study may play a significant role in initial platelet activation under pathological conditions.

While taken together our experimental findings support our  $\dot{\epsilon}$ -S mechanosome concept, there are some shortfalls in our experimental approach: (i) Chief among these is the reliance on a purely pharmacologic approach to investigate this phenomenon. This limitation is in part imposed by the rapidity of platelet functional responses under such acute velocity gradients and the intractability of human platelets to standard genetic manipulation. In addition,  $\dot{\epsilon}$ -S  $[\text{Ca}^{2+}]_c$  flux is triggered on a millisecond timescale making traditional approaches to the investigation of human platelet signal transduction difficult to employ. In future studies, we aim to utilize available transgenic mouse models to further explore the key platelet signaling regulators of  $\dot{\epsilon}$ -S, with a specific focus on the way in which PI3K C2 $\alpha$  regulates this mechanotransduction process. However, it must be born in mind that due to the relative difference in size of human versus mouse platelets the hemodynamic conditions required to trigger  $\dot{\epsilon}$ -S  $[\text{Ca}^{2+}]_c$  flux may be substantially different; (ii) Our use of time-averaged confocal imaging data to investigate very rapid platelet signaling under very high velocity flow is based on a compromise between  $\text{Ca}^{2+}$  probe (CAL520) signal strength (due to quantum yield and dye loading efficiency) and the need to derive high-speed data on platelet activation. This is in part due to the frame rate limitations of the resonant scanning system employed. By integrating CFD-based platelet trajectory modelling

with time-averaged imaging data, we were able to gain access to the millisecond change in platelet  $\text{Ca}^{2+}$  signaling. While powerful, this approach only enables interrogation of the ensemble average of platelet activation along predicted flow trajectories and does not enable the monitoring of single platelet responses. This is primarily a hardware limitation and may be overcome in the future through the use of ultrafast  $\mu$ -PIV-based imaging techniques; (iii) The generalized blood density and viscosity CFD model employed, while capable of accurately predicting overall platelet behavior within our model system(s), is not a non-Newtonian model per se and therefore does not consider the inertial effects of red blood cell and platelet mass on overall blood flow behavior; (iv) Finally, our conclusions are based on a purely synthetic reductionist approach utilizing microfluidic geometries to impose idealized supraphysiological hemodynamic gradients on blood components. In future studies, we aim to expand on this analysis and extract and model hemodynamic conditions found at pathological stenosis and within MCS pumping systems to investigate a role for  $\dot{\epsilon}$ -S in the pathology associated with these empirical systems.

## Conclusions

In conclusion, our working hypothesis is that  $\dot{\epsilon}$ -S represents the very earliest event in platelet activation under supraphysiological blood flow hemodynamics. In the context of overall platelet activation and aggregation, we posit that  $\dot{\epsilon}$ -S acts as a “priming mechanism” in response to initial flow acceleration, initiating platelet activation in free flow, allowing platelets to rapidly form immediate downstream adhesive interactions under the limiting effects of high relative flow velocities. This working model does not rule out a coincident role for  $\dot{\epsilon}$  during flow acceleration in promoting VWF unfolding [17] nor does it exclude a role for extreme  $\dot{\gamma}$  ( $>30,000 \text{ s}^{-1}$ ) in promoting concomitant VWF self-association and platelet aggregation [45], but rather posits that  $\dot{\epsilon}$ -S is coincident with these VWF-dependent processes and takes on an increasingly dominant role as hemodynamic gradients become more severe.

## Methods

### Symmetrical stepped stenosis microfluidic design

Stepped stenosis microchannel geometries were adapted from [46]. Symmetrical stenosis microfluidics (allowing for duplicate assay) were designed with entry and exit lengths of 6 mm and channel width of 600  $\mu\text{m}$ ; allowing for full flow development prior to stenosis (Additional file 1: Fig. S1A & B). A 30- $\mu\text{m}$  pillar array filter prior to the primary channel prevents debris reaching the symmetrical stenoses, which protrude 280  $\mu\text{m}$  into the



channel, with a gap distance between mirror image stenoses of 40  $\mu\text{m}$  and gap length of 20  $\mu\text{m}$  (Additional file 1: Fig. S1B). Entry angle ( $\theta_e$ ) variations (internal angles 20, 40, 60, and 80°) were generated keeping all other geometric parameters constant. Microfluidic arrays consisting of 14 independent channels per chip were fabricated allowing for high-throughput imaging and assay (Additional file 1: Fig. S1A). The entire microfluidic array was vacuum bonded to an underlying No. 1 borosilicate microscope coverslip via an integrated vacuum chuck allowing for easy reuse and coverslip changeover (Additional file 1: Fig. S1A). Hemodynamic control of the 14 independent on-chip microchannels was controlled by a custom built Tecan cavro centris syringe pump manifold (Tecan Group AG, Switzerland) allowing for serial or parallel perfusion experiments, sample management, and microchannel purging. Overall sample flow rates and sample switching control was driven by custom Python script.

#### Computational fluid dynamics—stepped stenosis microfluidics

3D CAD models of the stepped stenosis geometries on-chip were prepared using SolidWorks® (Dassault Systèmes, Vélizy-Villacoublay, France). Models were meshed with a mixture of tetrahedral and hexahedral unstructured elements (Pointwise, Inc. Fort Worth, Texas, USA) for CFD simulations. The total number of mesh elements ranged from 2.8 to 4.8 million. Mesh-independent studies were carried out for an index case to ensure adequate mesh resolutions. Finer mesh elements were used near the wall to ensure adequate resolution of the higher spatial velocity gradients there. CFD calculations were performed according to [47] with suitable modifications to the boundary conditions and a generalized blood density and viscosity model to accommodate the difference between coronary flow and present microfluidic devices. In brief, an in-house developed CFD solver based on OpenFOAM (v7, The OpenFOAM Foundation Ltd., UK) was used to simulate blood flow within each device [48]. A constant inflow, with matching flow rate at 200  $\mu\text{L}/\text{min}$ , was applied to the “INLET” (Additional file 1: Fig. S1A) of the device model. The velocity profile was allowed to fully develop with an extended model length upstream of the stenosis. Constant pressure was applied at the “Outlet” of the model. All simulations were performed for at least 1 s (i.e.,  $\sim 10$  washouts) to flush out any initial transient effect. Velocity, local  $\dot{\gamma}$  and  $\tau$  were extracted from tracing of individual (massless) particle paths. A total of 59 tracings (at resolutions of 1  $\mu\text{m}$  [near wall] to  $\sim 300$   $\mu\text{m}$  [centerline]) were computed (Fig. 1B). After an initial analyses, 3 subsamples (T1, T4, and T14) were reported to showcase critical behaviors (Fig. 1C–H).

#### Hyperbolic device design and assay

A hyperbolic-shaped microchannel geometry was used to examine the effect of strain/stress loading on human platelets under spatially uniform extensional strain rate [49]. Hyperbolic contraction channel microfluidics were designed with contraction length ( $L_h$ ) = 300  $\mu\text{m}$  + ( $L_g$ ) = 20  $\mu\text{m}$ ; contracting from a straight channel width ( $W_u$ ) = 600  $\mu\text{m}$  to ( $W_c$ ) = 40  $\mu\text{m}$  (Additional file 1: Fig. S4). At the end of the hyperbolic contraction, a sudden expansion ( $W_d$ ) = 600  $\mu\text{m}$  was used to investigate platelet  $[\text{Ca}^{2+}]_c$  flux recovery after the release of the fluidic force (Additional file 1: Fig. S4). All hyperbolic channel replicas had a constant height of  $z = 80$   $\mu\text{m}$ . Channels were incubated for 10 min with 2% w/v Pluronic F127 (Sigma Aldrich) and BSA (10%w/v) prior to platelet perfusion to prevent cell adhesion. Isolated human platelets were suspended in modified Tyrodes buffer (pH7.2) containing  $\text{CaCl}_2$  (1 mM),  $\text{MgCl}_2$  (1 mM), and 0.5%w/v methyl cellulose (Sigma Aldrich); final density = 1016  $\text{kg m}^{-3}$  and viscosity of  $0.004 \pm 0.015$  Pa.s [50]. Platelet  $[\text{Ca}^{2+}]_c$  dynamics were acquired for a duration of 30 s at a frame rate of 0.067 fps via resonant scanning confocal imaging (Nikon Plan Fluor  $\times 40$  WI/0.50 objective) using an Andor Zyla sCMOS camera (image scan size of  $512 \times 512$ ), with a focal point at  $z = 40$   $\mu\text{m}$ . Fluorescence image analysis was restricted to a 4- $\mu\text{m}$ -wide line scan running along the central axis of the microfluidic, representing  $0.1 \times W_c$  at which  $\dot{\epsilon}$  is considered uniform. Under these conditions, the hyperbolic region produces a uniform Hencky strain [51]  $\epsilon_H=2.7$ , i.e.,

$$\epsilon_H = \ln\left(\frac{w}{w_c}\right) \quad (1)$$

and Cauchy strain rate ( $\dot{\epsilon}$ ), based on the assumptions of; ideal hyperbolic flow, a spatially uniform viscosity of 0.004 Pa.s, channel height  $z = 80$   $\mu\text{m}$ , and  $Q = 12.5, 50, 200,$  and  $600$   $\mu\text{L}/\text{min}$ , of  $\dot{\epsilon} = \sim 318$   $\text{s}^{-1}, \sim 1309$   $\text{s}^{-1}, \sim 5458$   $\text{s}^{-1}$ , and  $\sim 16,013$   $\text{s}^{-1}$ , i.e.,

$$\dot{\epsilon} = \frac{Q}{L_c h} \left( \frac{kc}{w_c} - \frac{kd}{w} \right) \quad (2)$$

Based on the same assumptions, the flow extensional stresses  $\sigma_E = 1.3$  Pa, 5.3 Pa, 21.8 Pa, and 64.1 Pa, respectively.

#### Computational fluid dynamics—hyperbolic microfluidic

Solid Edge (Siemens PLM Software, USA) was used to extract the simulation domain from the 3D CAD model of the hyperbolic microfluidic channel. A hexahedral unstructured mesh with 2.3 million elements was generated using Pointwise, Inc. (Fort Worth, Texas, USA). Finer mesh elements were used around the domain's

centerline in the stenosis and downstream of it to investigate the impact of the hyperbolic geometry on the extensional strain rate and its gradient. A mesh convergence study was carried out to ensure adequate mesh resolution. The flow was assumed to be laminar, incompressible, and Newtonian with a viscosity of 0.004 Pa.s. The considered governing equations for conservation of mass and momentum were as per [49]. Numerical simulation of the flow through the hyperbolic channel was performed using OpenFOAM v8 (The OpenFOAM Foundation Ltd., UK). The steady-state solver for incompressible flow simpleFoam, which is based on the SIMPLE (Semi-Implicit Method for Pressure Linked Equations) algorithm, was chosen for the simulations. A constant uniform inflow was applied at the “Inlet” of the model, the model length upstream was sufficient to allow for fully developed flow in the hyperbolic segment. Constant pressure was applied at the “Outlet” of the model. No-slip condition at the solid walls was imposed. The simulations were performed for four different inflow rates:  $Q = 12.5 \mu\text{L}/\text{min}$ ,  $50 \mu\text{L}/\text{min}$ ,  $200 \mu\text{L}/\text{min}$ , and  $600 \mu\text{L}/\text{min}$ . An open-source, multi-platform data analysis and visualization application ParaView 5.6.0 (Sandia National Laboratories, Kitware Inc, Los Alamos National Laboratory) was used for visualization and extraction of the stream-wise velocity along the centerline of the model. Python code was used to calculate the extensional strain rate and its gradient for each of the considered cases.

#### Microfluidic fabrication

All microfluidic devices were fabricated using established soft photolithography methods [46]. Briefly, using maskless lithography (MLA 150, Heidelberg instruments), a master template was patterned onto a 4-in. silicon wafer using SU-8 3050 photoresist (MicroChem Corp.) to produce defined channel features with a height of  $100 \mu\text{m}$  for the symmetric step and  $80 \mu\text{m}$  for the hyperbolic geometry. PDMS (Sylgard 184) mixed with a curing agent in a 1:10 ratio by weight, degassed in a vacuum desiccator, and cast on the master template and cured at  $130^\circ\text{C}$  in a convection oven for 15 min. The cured PDMS was peeled off the mold, cut to size, and punched with a 0.75-mm hole at the inlets, outlets, and vacuum chuck, before being reversibly sealed onto a No. 1 borosilicate microscope coverslip. Microfluidic chips were re-cycled between use via sonication in 20% Extran MA05 (Merck Millipore), followed by sonication in DI water, and baked in a convection oven at  $110^\circ\text{C}$  following a final DI rinse.

#### Blood collection and handling

Ethics approval was obtained from Monash University Human Research Ethics Committee. Blood from healthy consenting volunteers was withdrawn using a 19G

butterfly needle into syringes containing either acid citrate dextrose (ACD) [ratio of 6:1 (blood/ACD)] for platelet and red blood cell isolation or 800 U/mL Lepirudin® for VWF aggregation assay and FACS analysis. Samples were gently inverted to mix anticoagulant, transferred to 50-mL Falcon® tubes, and allowed to rest for 10 min at  $37^\circ\text{C}$  prior to use.

#### Platelet isolation

Platelet isolation from human whole blood was carried out as per [52]. Briefly, human whole blood collected in ACD was supplemented with 0.005 U/mL apyrase before incubation at  $37^\circ\text{C}$  for 10 min. PRP was isolated by centrifugation at  $200\times g$  for 15 min, followed by another centrifugation at  $1700\times g$  for 7 min, where platelet poor plasma (PPP) was removed and platelet pellet resuspended in an equal volume of platelet washing buffer (PWB) [4.3 mM  $\text{K}_2\text{HPO}_4$ , 4.3 mM  $\text{Na}_2\text{HPO}_4$ , 24.3 mM  $\text{NaH}_2\text{PO}_4$ , 113 mM NaCl, 5.5 mM D-glucose, and 10 mM theophylline, (pH 6.5) containing 0.5% w/v BSA, 0.01 U/mL apyrase, and 800 U/mL hirudin]. A final centrifugation was performed on the platelet suspension at  $1500\times g$  for 7 min and the platelet pellet was resuspended in PWB (supplemented with 0.02 U/mL apyrase) to achieve a platelet concentration of  $300 \times 10^9/\text{L}$ . For CellTracker Green (CMFDA) experiments, isolated platelets were rested at  $37^\circ\text{C}$  for 30 min with  $10 \mu\text{M}$  CMFDA. Following the incubation period, CMFDA-labelled platelets were reconstituted with washed RBC (40% final hematocrit, Hct) prior to perfusion through the device (Fig. S2B).

#### Platelet $\text{Ca}^{2+}$ (CAL520) assay

Platelet calcium assay was adapted from published methods [52, 53]. Washed platelets ( $300 \times 10^9/\text{L}$ ) were loaded with  $1.25 \mu\text{M}$  CAL520 (2-aminophenoxy) ethane- $\text{N,N,N',N'}$ -tetraacetic acid tetra(acetoxymethyl) ester (JOMAR Life Research) for 45 min at  $37^\circ\text{C}$ . CAL520-loaded platelets in Tyrodes +  $1\text{mM}$   $\text{Ca}^{2+}/\text{Mg}^{2+}$  were then reconstituted with washed RBC (40% final hematocrit; Hct) prior to perfusion through stepped stenosis microfluidics. Hct and platelet counts were performed by full blood analysis using Cell-Dyn Emerald® hematology analyzer (Abbott Diagnostics).  $[\text{Ca}^{2+}]_c$  dynamics were acquired for a duration of 30 s with a “no delay” interval for highest speed via resonant scanning confocal imaging (Nikon Plan Fluor  $\times 40$  WI/0.50 objective) using an Andor Zyla sCMOS camera at 15 frames per second (image scan size of  $512 \times 512$ ). All image analysis was performed off-line in FIJI. The corrected fluorescence values (F) for each region of interest (ROI) or line scan profile were converted into pseudo-ratio values according to:

$$[Ca^{2+}]_c = K_d \left[ \frac{(F - F_{min})}{(F - F_{max})} \right] [K_d \text{ CAL520} = 320 \text{ nM}] \quad (3)$$

where  $F_{min}$  was derived for independent platelet flow experiments in which CAL520-loaded platelets were treated with 50  $\mu\text{M}$  DM-BAPTA-AM (Sigma Aldrich) and resuspended in Tyrodes buffer supplemented with 5 mM EGTA and  $F_{max}$  derived for independent platelet flow experiments in which CAL520-loaded platelets were treated with 2.5  $\mu\text{M}$  A23187 (Sigma Aldrich) and resuspended in Tyrodes buffer supplemented with 5 mM  $\text{CaCl}_2$ .

### CFD-directed $\text{Ca}^{2+}$ image analysis

Image analyses were performed off-line using a custom macro in FIJI (ImageJ). To analyze trajectory-dependent changes in platelet  $[\text{Ca}^{2+}]_c$  flux, resonant scanning confocal image timelapse stacks were imported into FIJI using Bio-Formats. Stacks were background corrected and a  $z$ -projection (sum slices) generated to create a time-averaged image (304 total frames).  $Z$ -projections were thresholded using Huang's fuzzy logic (Light). CFD-derived platelet trajectories were plotted in FIJI as concatenated  $x,y$  coordinates using the makeLine ( $x1, y1, x2, y2, \text{lineWidth}$ ) macro (line width = 5  $\mu\text{m}$ ) and imported into the FIJI ROI manager. Trajectories were overlaid on  $z$ -projections from ROI manager. To align trajectories three fiducial markers located at the base and top of the microfluidic features were included in the ROI set and manually aligned with the imaging data. Multi-plot line scan profiles using the CFD-defined trajectories were analyzed and intensity data extracted. This process was carried out for  $F, F_{min}$ , and  $F_{max}$  data sets and  $[\text{Ca}^{2+}]_c$  along profile scans assessed. To gain a statistically significant sample size across multiple blood/platelet donors, a ROI subset was assessed for select CFD trajectories for each donor. Then, 10- $\mu\text{m}$ -diameter ROIs were defined by their  $x,y$  coordinate positions equivalent to the start of acceleration (Acc1), the midpoint of acceleration (Acc2), the endpoint of acceleration adjacent to the stenosis apex (Acc3), the midpoint of stenosis apex (Apex), and reference points positioned 3 mm up and downstream of the apex midpoint were overlaid on the  $z$ -projected data sets. Fluorescence intensities for each ROI were determined for each using the Analyze/measure function in FIJI. This ROI-dependent analysis was performed for each ROI across  $F, F_{min}$ , and  $F_{max}$  samples and  $[\text{Ca}^{2+}]_c$  determined. The analysis Macro, CFD trajectory, and ROI coordinates are available on request.

### Red blood cell isolation

RBC isolation was carried out as per [52]. Briefly, human whole blood was collected in ACD and rested at 37 °C for

10 min. Apyrase (0.005 U/mL) was added to the blood to remove any ADP secreted during venipuncture, and centrifuged at 200 $\times g$  for 15 min. The platelet-rich plasma (PRP) supernatant along with the buffy coat was carefully discarded by aspiration. The remaining packed RBC were washed 3 $\times$  with an equal volume of 1 $\times$  Tyrode's buffer [10 mM Hepes, 12 mM  $\text{NaHCO}_3$ , 137 mM NaCl, 2.7 mM KCl, and 5 mM glucose (pH 7.4)] and mixed by gentle inversion and subsequently centrifuged at 1700 $\times g$  for 7 min (50 mL) to pack the erythrocyte phase.

Where fixed RBC were required, packed RBC were resuspended in an equal volume of 0.16%v/v glutaraldehyde in 1 $\times$  Tyrodes (1:1v/v) to a final concentration of 0.08%v/v and incubated for 10 min at room temperature. Fixed RBC were subsequently washed 5 $\times$  (as above) with resuspension in an equal volume of supplemented 1 $\times$  Tyrode's buffer (+1 mM  $\text{CaCl}_2$  + 0.5 % w/v BSA). The final packed RBC suspension was supplemented with 800 U/mL hirudin and 0.02 U/mL apyrase and allowed to rest for 30 min at 37 °C. Immediately prior to reconstitution with isolated platelets, the RBC suspension was supplemented with a further 0.02 U/mL apyrase to prevent erythrocyte derived ADP from activating the isolated platelet suspension.

### VWF microfluidic aggregation assay

Platelet aggregation was performed as previously described [46]. Microchannels were selectively derivatized with human VWF (10  $\mu\text{g}/\text{ml}$ ; isolated from Biostate CSL Ltd) for 10 min, such that only the peak stenosis and downstream stenosis face were coated, to allow for focal platelet capture and adhesion to the PDMS surface (Fig. S1C & D). VWF was manually injected into the channel outlet (Fig. S1A) to coat downstream up until the apex of the stenosis geometry. Following 10-min incubation, VWF was aspirated from the outlet (Fig. S1A) to remove any excess and the PDMS was vacuum sealed onto a new isopropanol-washed coverslip. The channels were then subsequently blocked with 2% w/v BSA via the channel inlet for 10 min to passivate the non-VWF-coated upstream regions, prior to wash out with unmodified tyrodes buffer pH 7.4. Hirudinized human whole blood was incubated with the lipophilic membrane dye DiOC<sub>6</sub> (1  $\mu\text{g}/\text{mL}$ ) for 10 min at 37 °C prior to device perfusion. Where drug treatments were required, blood samples were treated with the reagent and incubated for 10 min at 37 °C prior to device perfusion. Platelet aggregation at the stenosis was monitored via epifluorescence at 1 fps for 180 s (Nikon Ti-E microscope Plan Fluor  $\times$  20/0.50 objective with Andor Zyla sCMOS detector). Aggregate size was assessed as per [46] and expressed as mid-plane surface area in square micrometers.

### FACS analyses

Prior to perfusion, microfluidic devices were coated with 2% w/v BSA for 10 min prior to wash out with unmodified tyrodes buffer pH 7.4. Hirudin anticoagulated whole blood was either perfused through the external syringe pump line as a baseline control (no microfluidic perfusion) or  $\theta_e = 80^\circ$  geometry at  $Q = 200 \mu\text{L}/\text{min}$ , or no perfusion as a resting control. Each sample was diluted 1:10 in  $1\times$  Tyrode's buffer ( $+1 \text{ mM CaCl}_2 + 0.5\% \text{ BSA w/v}$ ) and  $5 \mu\text{L}$  of the diluted sample was immediately transferred to their respective Eppendorf tubes containing  $\alpha\text{-CD42bAPC}$  (Becton Dickinson), and either  $5 \mu\text{L}$  PAC-1 FITC (Becton Dickinson) or  $5 \mu\text{L}$   $\alpha\text{-P-selectin-PE}$  (Life Technologies). The tube containing positive control was activated with  $40 \mu\text{M}$  ADP and all samples were let to rest for 15 min. Reaction was stopped by adding  $600 \mu\text{L}$   $1\times$  Tyrode's buffer and immediately transferred to  $12 \times 75 \text{ mm}$  Falcon<sup>®</sup> polystyrene test tubes, and all samples were assessed within a 2-h window. Platelets were identified by light scatter characteristics and confirmed by CD42b expression. Positive controls were used to adjust voltages. Acquisition was performed on a BD FACSCanto-II (Becton Dickinson) that was routinely calibrated with Calibrite beads in conjunction with FACSComp Version 5.1 software (Becton Dickinson). The results were analyzed with FlowLogic 7.2.1 flow cytometric analysis software.

### Statistical analysis

Two-way ANOVA and Tukey's multiple comparisons test were performed in GraphPad Prism. Nonlinear curve fitting of microfluidic aggregation experiments was fitted by least squares regression using an [Agonist] vs. response Variable slope (four parameters; no weighting) model with the Bottom constrained to a constant = 0. Where indicated statistical significance is defined as \*\*\*\*  $P < 0.0001$ ; \*\*\*  $P = 0.0001$  to  $0.001$ ; \*\*  $P = 0.001$  to  $0.01$ ; \*  $P = 0.01$  to  $0.05$ ; ns  $P \geq 0.05$ .

### Supplementary Information

The online version contains supplementary material available at <https://doi.org/10.1186/s12915-022-01274-7>.

**Additional file 1: Fig S1.** High-throughput stenosis microfluidics platform & platelet aggregation assay method schema. **Fig S2.**  $\text{Ca}^{2+}$  trajectory sampling and hemodynamics. **Fig S3.** Effect of stenosis entry geometry on trajectory dependent hemodynamics and platelet function. **Fig S4.** Hyperbolic microfluidic geometry & platelet  $[\text{Ca}^{2+}]_c$  assay schema. **Fig S5.** Effect of NF449 and Cbx on platelet aggregation.

### Acknowledgements

The authors acknowledge Professors Elizabeth Gardiner, Peter Barlis, Harshal Nandurkar, Huyen Tran, and Mrs. Volga Tarlac, and Dr. Pia Larsson for helpful discussions, manuscript review, and technical advice. We thank the staff at the

Australian Centre for Blood Diseases for blood collection and donations. The authors acknowledge the facilities of Monash Micro Imaging, Monash University. Devices were fabricated at the Micro Nano Research Facility, RMIT University.

### Authors' contributions

NAZA developed experimental assays, fabricated devices, and co-wrote the manuscript; EKWP, MT, CL, and ASHO carried out CFD simulations; CS and AM designed microfluidic systems; FA and IM developed and fabricated hyperbolic microfluidics; RJB and FJT contributed to experimental work; XM and PET developed and synthesized PI3K C2 $\alpha$  inhibitors; JRH developed PI3K C2 $\alpha$  inhibitors and co-supervised the project; WSN developed the experimental design and concepts, supervised the project, and wrote the manuscript. MT and FA contributed equally to the work. All authors read and approved the final manuscript.

### Funding

Sustaining and Strengthening Merit-Based Access to National Computational Infrastructure (NCI) LIEF grant LE190100021 (EKWP). National Health & Medical Research Council Project grant APP144210(JRH, PET & WSN). National Health & Medical Research Council Development grant APP1153716(WSN & JRH).

### Availability of data and materials

The datasets supporting the conclusions of this article are included within the article (and its supplementary files).

### Declarations

#### Ethics approval and consent to participate

Ethics approval was obtained from Monash University Human Research Ethics Committee.

#### Competing interests

The authors declare that they have no competing interests.

#### Author details

<sup>1</sup>The Australian Centre for Blood Diseases, Monash University, Melbourne, VIC 3004, Australia. <sup>2</sup>Department of Medicine, St Vincent's Hospital, Melbourne Medical School, Faculty of Medicine, Dentistry & Health Sciences, The University of Melbourne, Fitzroy, VIC 3065, Australia. <sup>3</sup>School of Engineering, RMIT University, La Trobe Street, Melbourne, VIC 3004, Australia. <sup>4</sup>Department of Mechanical Engineering, Faculty of Engineering and Information Technology, The University of Melbourne, Melbourne, VIC 3010, Australia. <sup>5</sup>Medicinal Chemistry, Monash Institute of Pharmaceutical Sciences, Monash University, Parkville, VIC 3052, Australia. <sup>6</sup>CFD Methodology Group, Scuderia AlphaTauri F1, Bicester OX26 4LD, UK.

Received: 1 September 2021 Accepted: 7 March 2022

Published online: 24 March 2022

### References

- Bark DL Jr, Ku DN. Wall shear over high degree stenoses pertinent to atherothrombosis. *J Biomech.* 2010;43(15):2970–7.
- Ruggeri ZM. Mechanisms of shear-induced platelet adhesion and aggregation. *Thromb Haemost.* 1993;70(1):119–23.
- Tovar-Lopez FJ, Rosengarten G, Nasabi M, Sivan V, Khoshmanesh K, Jackson SP, et al. An investigation on platelet transport during thrombus formation at micro-scale stenosis. *PLoS One.* 2013;8(10):e74123.
- Mody NA, Lomakin O, Doggett TA, Diacovo TG, King MR. Mechanics of transient platelet adhesion to von Willebrand factor under flow. *Biophys J.* 2005;88(2):1432–43.
- Ju L, McFadyen JD, Al-Daher S, Alwis I, Chen Y, Tonnesen LL, et al. Compression force sensing regulates integrin  $\alpha\text{IIb}\beta\text{3}$  adhesive function on diabetic platelets. *Nat Commun.* 2018;9(1):1087.
- Nesbitt WS, Westein E, Tovar-Lopez FJ, Tolouei E, Mitchell A, Fu J, et al. A shear gradient-dependent platelet aggregation mechanism drives thrombus formation. *Nat Med.* 2009;15(6):665–73.

7. Strony J, Beaudoin A, Brands D, Adelman B. Analysis of shear stress and hemodynamic factors in a model of coronary artery stenosis and thrombosis. *Am J Physiol*. 1993;265(5 Pt 2):H1787–96.
8. Purvis NB Jr, Giorgio TD. The effects of elongational stress exposure on the activation and aggregation of blood platelets. *Biorheology*. 1991;28(5):355–67.
9. Nesbitt WS, Kulkarni S, Giuliano S, Goncalves I, Dopheide SM, Yap CL, et al. Distinct glycoprotein Ib/VI and integrin alpha IIb beta 3-dependent calcium signals cooperatively regulate platelet adhesion under flow. *J Biol Chem*. 2002;277(4):2965–72.
10. Yap CL, Anderson KE, Hughan SC, Dopheide SM, Salem HH, Jackson SP. Essential role for phosphoinositide 3-kinase in shear-dependent signaling between platelet glycoprotein Ib/VI and integrin alpha IIb beta 3. *Blood*. 2002;99(1):151–8.
11. Mountford JK, Petitjean C, Putra HW, McCafferty JA, Setiabakti NM, Lee H, et al. The class II PI 3-kinase, PI3KC2a, links platelet internal membrane structure to shear-dependent adhesive function. *Nat Commun*. 2015;6:6535.
12. Fox JE. The platelet cytoskeleton. *Thromb Haemost*. 1993;70(6):884–93.
13. Ruggeri ZM. Platelet adhesion under flow. *Microcirculation*. 2009;16(1):58–83.
14. Dopheide SM, Maxwell MJ, Jackson SP. Shear-dependent tether formation during platelet translocation on von Willebrand factor. *Blood*. 2002;99(1):159–67.
15. Huang PY, Hellums JD. Aggregation and disaggregation kinetics of human blood platelets: Part II. Shear-induced platelet aggregation. *Biophys J*. 1993;65(1):344–53.
16. Schneider SW, Nuschele S, Wixforth A, Gorzelanny C, Alexander-Katz A, Netz RR, et al. Shear-induced unfolding triggers adhesion of von Willebrand factor fibers. *Proc Natl Acad Sci U S A*. 2007;104(19):7899–903.
17. Singh I, Themistou E, Porcar L, Neelamegham S. Fluid shear induces conformation change in human blood protein von Willebrand factor in solution. *Biophys J*. 2009;96(6):2313–20.
18. Kroll MH, Hellums JD, McIntire LV, Schafer AI, Moake JL. Platelets and shear stress. *Blood*. 1996;88(5):1525–41.
19. Hassock SR, Zhu MX, Trost C, Flockerzi V, Authi KS. Expression and role of TRPC proteins in human platelets: evidence that TRPC6 forms the store-independent calcium entry channel. *Blood*. 2002;100(8):2801–11.
20. Coste B, Mathur J, Schmidt M, Earley TJ, Ranade S, Petrus MJ, et al. Piezo1 and Piezo2 are essential components of distinct mechanically activated cation channels. *Science*. 2010;330(6000):55.
21. Ilkan Z, Wright JR, Goodall AH, Gibbins JM, Jones CI, Mahaut-Smith MP. Evidence for shear-mediated Ca(2+) entry through mechanosensitive cation channels in human platelets and a megakaryocytic cell line. *J Biol Chem*. 2017;292(22):9204–17.
22. Gnanasambandam R, Ghatak C, Yasmann A, Nishizawa K, Sachs F, Ladokhin AS, et al. GsMTx4: mechanism of inhibiting mechanosensitive ion channels. *Biophys J*. 2017;112(1):31–45.
23. Syeda R, Xu J, Dubin AE, Coste B, Mathur J, Huynh T, et al. Chemical activation of the mechanotransduction channel Piezo1. *Elife*. 2015;4:e07369.
24. Mousawi F, Peng H, Li J, Ponnambalam S, Roger S, Zhao H, et al. Chemical activation of the Piezo1 channel drives mesenchymal stem cell migration via inducing ATP release and activation of P2 receptor purinergic signaling. *Stem Cells*. 2020;38(3):410–21.
25. Miyamoto T, Mochizuki T, Nakagomi H, Kira S, Watanabe M, Takayama Y, et al. Functional role for Piezo1 in stretch-evoked Ca<sup>2+</sup> influx and ATP release in urothelial cell cultures. *J Biol Chem*. 2014;289(23):16565–75.
26. Hechler B, Lenain N, Marchese P, Vial C, Heim V, Freund M, et al. A role of the fast ATP-gated P2X1 cation channel in thrombosis of small arteries in vivo. *J Exp Med*. 2003;198(4):661–7.
27. Taylor KA, Wright JR, Vial C, Evans RJ, Mahaut-Smith MP. Amplification of human platelet activation by surface pannexin-1 channels. *J Thromb Haemost*. 2014;12(6):987–98.
28. Selvadurai MV, Brazilek RJ, Moon MJ, Rinckel JY, Eckly A, Gachet C, et al. The PI 3-kinase PI3KC2a regulates mouse platelet membrane structure and function independently of membrane lipid composition. *FEBS Lett*. 2019;593(1):88–96.
29. Selvadurai MV, Moon MJ, Mountford SJ, Ma X, Zheng Z, Jennings IG, et al. Disrupting the platelet internal membrane via PI3KC2a inhibition impairs thrombosis independently of canonical platelet activation. *Sci Transl Med*. 2020;12(553):ear8430.
30. Buyan A, Cox CD, Barnoud J, Li J, Chan HSM, Martinac B, et al. Piezo1 forms a buoyan specific, functionally important interactions with phosphoinositides and cholesterol. *Biophys J*. 2020;119(8):1683–97.
31. Valet C, Chicanne G, Severac C, Chaussade C, Whitehead MA, Cabou C, et al. Essential role of class II PI3K-C2a in platelet membrane morphology. *Blood*. 2015;126(9):1128–37.
32. Boyanova D, Nilla S, Birschmann I, Dandekar T, Dittrich M. PlateletWeb: a systems biologic analysis of signaling networks in human platelets. *Blood*. 2012;119(3):e22–34.
33. Burkhart JM, Vaudel M, Gambaryan S, Radau S, Walter U, Martens L, et al. The first comprehensive and quantitative analysis of human platelet protein composition allows the comparative analysis of structural and functional pathways. *Blood*. 2012;120(15):e73–82.
34. Botello-Smith WM, Jiang W, Zhang H, Ozkan AD, Lin YC, Pham CN, et al. A mechanism for the activation of the mechanosensitive Piezo1 channel by the small molecule Yoda1. *Nat Commun*. 2019;10(1):4503.
35. Forsyth AM, Wan J, Owruksy PD, Abkarian M, Stone HA. Multiscale approach to link red blood cell dynamics, shear viscosity, and ATP release. *Proc Natl Acad Sci U S A*. 2011;108(27):10986–91.
36. Wang S, Chennupati R, Kaur H, Iring A, Wettschreck N, Offermanns S. Endothelial cation channel PIEZO1 controls blood pressure by mediating flow-induced ATP release. *J Clin Invest*. 2016;126(12):4527–36.
37. Romero LO, Massey AE, Mata-Daboian AD, Sierra-Valdez FJ, Chauhan SC, Cordero-Morales JF, et al. Dietary fatty acids fine-tune Piezo1 mechanical response. *Nat Commun*. 2019;10(1):1200.
38. Cox CD, Gottlieb PA. Amphipathic molecules modulate PIEZO1 activity. *Biochem Soc Trans*. 2019;47(6):1833–42.
39. Foster FM, Traer CJ, Abraham SM, Fry MJ. The phosphoinositide (PI) 3-kinase family. *J Cell Sci*. 2003;116(Pt 15):3037–40.
40. Guo YR, MacKinnon R. Structure-based membrane dome mechanism for Piezo mechanosensitivity. *Elife*. 2017;6:e33660.
41. Wu J, Young M, Lewis AH, Martfeld AN, Kalmeta B, Grandl J. Inactivation of mechanically activated Piezo1 ion channels is determined by the C-terminal extracellular domain and the inner pore helix. *Cell Rep*. 2017;21(9):2357–66.
42. Rolf MG, Brearley CA, Mahaut-Smith MP. Platelet shape change evoked by selective activation of P2X1 purinoceptors with alpha,beta-methylene ATP. *Thromb Haemost*. 2001;85(2):303–8.
43. Bluestein D, Niu L, Schoephoerster RT, Dewanjee MK. Fluid mechanics of arterial stenosis: relationship to the development of mural thrombus. *Ann Biomed Eng*. 1997;25(2):344–56.
44. Sing CE, Alexander-Katz A. Elongational flow induces the unfolding of von Willebrand factor at physiological flow rates. *Biophys J*. 2010;98(9):L35–7.
45. Colace TV, Diamond SL. Direct observation of von Willebrand factor elongation and fiber formation on collagen during acute whole blood exposure to pathological flow. *Arterioscler Thromb Vasc Biol*. 2013;33(1):105–13.
46. Brazilek RJ, Tovar-Lopez FJ, Wong AKT, Tran H, Davis AS, McFadyen JD, et al. Application of a strain rate gradient microfluidic device to von Willebrand's disease screening. *Lab Chip*. 2017;17(15):2595–608.
47. Gijssen F, Katagiri Y, Barlis P, Bourantas C, Collet C, Coskun U, et al. Expert recommendations on the assessment of wall shear stress in human coronary arteries: existing methodologies, technical considerations, and clinical applications. *Eur Heart J*. 2019;40(41):3421–33.
48. Poon EKW, Thondapu V, Hayat U, Barlis P, Yap CY, Kuo PH, et al. Elevated blood viscosity and microcirculation resulting from coronary stent malapposition. *J Biomech Eng*. 2018;140(5). <https://doi.org/10.1115/1.4039306>.
49. Oliveira MSN, Alves MA, Pinho FT, McKinley GH. Viscous flow through microfabricated hyperbolic contractions. *Exp Fluids*. 2007;43(2):437–51.
50. Piergiovanni M, Galli V, Holzner G, Stavrakis S, DeMello A, Dubini G. Deformation of leukaemia cell lines in hyperbolic microchannels: investigating the role of shear and extensional components. *Lab Chip*. 2020;20(14):2539–48.
51. Ober TJ, Haward SJ, Pipe CJ, Soulages J, McKinley GH. Microfluidic extensional rheometry using a hyperbolic contraction geometry. *Rheol Acta*. 2013;52(6):529–46.

52. Nesbitt WS, Harper IS, Schoenwaelder SM, Yuan Y, Jackson SP. A live cell micro-imaging technique to examine platelet calcium signaling dynamics under blood flow. *Methods Mol Biol.* 2012;788:73–89.
53. Heemskerk JW, Willems GM, Rook MB, Sage SO. Ragged spiking of free calcium in ADP-stimulated human platelets: regulation of puff-like calcium signals in vitro and ex vivo. *J Physiol.* 2001;535(Pt 3):625–35.

### **Publisher's Note**

Springer Nature remains neutral with regard to jurisdictional claims in published maps and institutional affiliations.

**Ready to submit your research? Choose BMC and benefit from:**

- fast, convenient online submission
- thorough peer review by experienced researchers in your field
- rapid publication on acceptance
- support for research data, including large and complex data types
- gold Open Access which fosters wider collaboration and increased citations
- maximum visibility for your research: over 100M website views per year

**At BMC, research is always in progress.**

Learn more [biomedcentral.com/submissions](https://biomedcentral.com/submissions)

